Brachytherapy Strand Localization Using Average-Reflected-Power Ultrasound Data and Echogenic EchoStrand^{TM}

by

Jack Zheng

A THESIS SUBMITTED IN PARTIAL FULFILLMENT OF
THE REQUIREMENTS FOR THE DEGREE OF

BACHELOR OF SCIENCE

in

The Faculty of Science

(Honors Biophysics)

THE UNIVERSITY OF BRITISH COLUMBIA

(Vancouver)

August 2010

Abstract

This project aims to determine if average-reflected-power ultrasound imaging and echogenic EchoStrand^{TM} is able to improve real-time brachytherapy strand localization on the ultrasound. The first part of the experiment compares both regular and EchoStrand^{TM} image intensities at various orientations and the ability to attribute these strands to different image planes. The second part directly compares the abilities of average-reflected-image imaging and regular B-Mode imaging in contrasting both strand types against a noisy background.

The EchoStrand^{TM} is visually and quantitatively found to give a stronger intensity response and better contrast to background noise ratio than regular strands particularly at non-parallel strand orientations. Both strands can be attributed to associated image plane with a small degree of error, though this was more difficult for regular strands at non-parallel orientations. The average-reflected-power imaging technique greatly enhances the contrast to background of both strands across all orientations compared with regular B-Mode imaging. Overall, the combination of EchoStrand^{TM} and average-reflected-power imaging is found to improve the strand localization abilities of the ultrasound. A clinical study can be conducted to further build on the conclusions arrived in this project.

Jack Zheng - jackz@interchange.ubc.ca

Table of Contents

List of Figures

Acknowledgements

I would like to thank my supervisor Dr. Tim Salcudean along with Dr. Mehdi Moradi (Post-doctoral Fellow) from the UBC Electrical and Computer Engineering Department for their tremendous guidance and support. Special thanks to Xu Wen for his work in developing the average-reflected-power imaging method as well as other members of the UBC Robotics and Control Laboratory for their contribution to the success of this project.

Dedication

To my parents for instilling in me the drive to continually learn and grow. Thank you.

Chapter 1

Introduction

Prostate cancer is the most commonly diagnosed form of cancer in Canadian men and is the third leading cause of male cancer deaths. It is estimated that 25,500 new cases of prostate cancer will be diagnosed in 2009 alone and 4,400 Canadian men will die from it[6].

Brachytherapy has increasingly gained acceptance as a minimally invasive procedure that delivers successful treatment outcomes against prostate cancer[10]. In brachytherapy, rows of radioactive metal seeds are sutured together into long strands which are then implanted into a patient's prostate. The radioactive seeds within each strand locally irradiate and kill surrounding cancerous tissues. The implantation process is guided by a transrectal ultrasound probe (TRUS)[11].

The two goals in brachytherapy are to deliver an adequate dose of radiation to cancerous tissues of the prostate while minimizing radiation to the surrounding organs of the urethra and rectum. Successfully achieving these reduces both post-operation recurrence rates and complications[11]. Radioactive seed positions are implanted in a pattern that best meet these goals.

However, insertion errors can lead to large deviations between where the seeds are actually placed and where they should be placed. These errors create a drastically different dosimetry profile and negatively impact the outcome of the procedure. Being able to modify the plan during the procedure is required to minimize the effects of these errors[7, 13]. To perform these modifications accurately, an up-to-date dosimetry profile must be calculated based on the positions of the already implanted seeds. This type of calculation is called real-time dosimetry[11].

Accurate real-time dosimetry depends on the ability to localize the already implanted radioactive seeds and the most convenient way of achieving this is to use the TRUS probe. However, it is difficult to localize individual seeds on the ultrasound due to the small seed size and high background noise from speckles and shadow artifacts in the surrounding tissue[7]. Localizing the strands is also an issue as the spacer material that make up the majority of the strand give a very dim intensity response.

Though seed and strand localization are difficult to accomplish in traditional ultrasound, a novel image enhancement technique developed at the UBC Robotics and Control Laboratory using average-reflected-power imaging has proven to be promising in making this process easier[23].

In addition, a new type of brachytherapy strand is now available made from highly acoustically-reflective spacer materials. The special composition of these EchoStrands^{TM} allows the entire

strand to be visualized on ultrasound images.

This project aims to determine if the use of average-reflected-power imaging and EchoStrands^{TM} can form the basis for accurate ultrasound strand localization. The ability to localize regular brachytherapy strands and EchoStrands^{TM} using traditional ultrasound B-Mode imaging and average-reflected-power imaging is also compared.

If a significant improvement in strand localization is found, subsequent experiments can then be conducted in a clinical study to determine the full viability of seed localization using EchoStrands^{TM} and average-reflected-power imaging.

Chapter 2

Brachytherapy

2.1 Background

In treating prostate cancer, traditional options have included radical prostatectomy, external beam radiation and hormonal therapy, but over the last two decades, brachytherapy has increasingly gained acceptance as a minimally invasive treatment option[10]. Brachytherapy can serve both as a complete course of treatment and be complemented by external beam radiation therapy[24].

The most important advantage of brachytherapy is its ability to deliver extremely localized radiation to specific targets in the body. This allows much higher doses to be delivered to target tissues than those achievable by external beam radiation therapy[4]. A high dose rate both decreases the likelihood of cancer recurrence and treatment time.

Brachytherapy is associated with lower morbidity rates and leads to fewer incidents of sexual dysfunction and incontinence as compared to other treatment procedures[4, 24]. A greater preservation of sexual potency is also observed from brachytherapy as a great majority of individuals can continue to engage in sexual activities following the procedure[18].

Major acute complications from brachytherapy are also extremely rare. Events such as bleeding that require transfusion, admission to the intensive care unit and death have not being noted in literature[4].

Brachytherapy has existed in some form since the 1960s but it was only in 1985 that the modern method of trans-perineal ultrasound guided brachytherapy was first performed by Dr. Blasko and Ragde. Over the past 25 years, technological and procedural developments have greatly increased the efficiency and quality of the procedure but the basic approach remains relatively the same[4].

Modern brachytherapy is divided into two stages. First, computerized treatment planning is conducted to determine the proper number, strengths and positions of the radioactive seed sources. Second, the actual seed implantation procedure takes place[11]. The Brachytherapy procedures presented in the following sections are based on guidelines found in review articles written by the American Brachytherapy Association and other research centers[4, 11, 24].

2.2 Brachytherapy Planning

The planning stage for the brachytherapy procedure can be done from days/weeks before the implantation procedure to immediately proceeding it. Planning consists of performing an ultrasound volume study on the prostate region. The prostate and other organs are then delineated from the volume study images. Seed positions are finally determined through an optimization procedure to give the desired radiation dosage to the target organs.

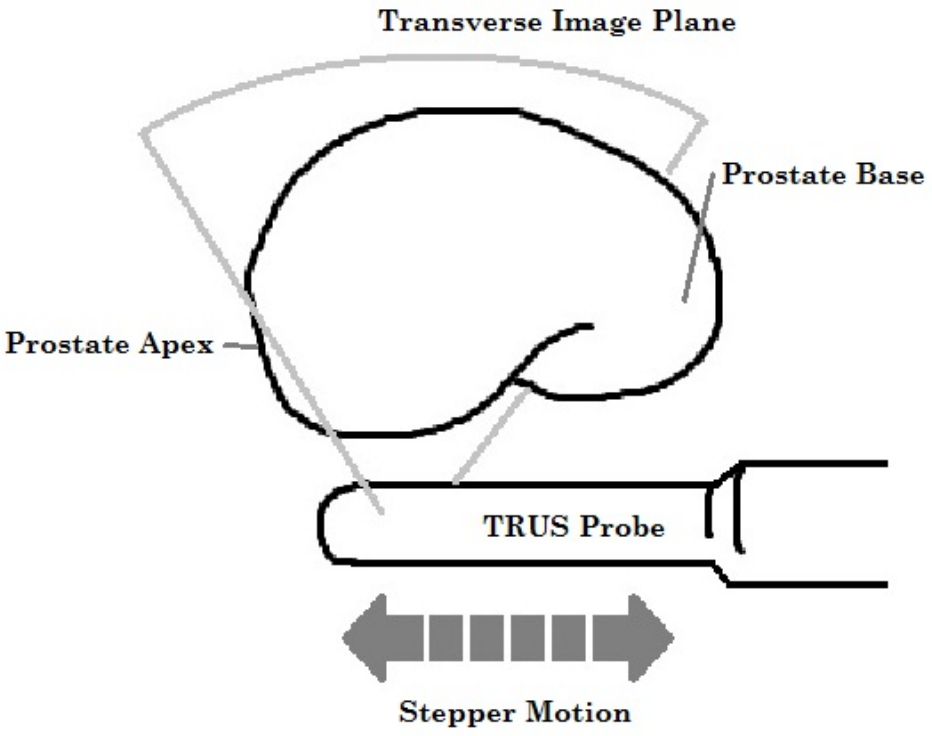

Figure 2.1: To perform the volume study, the TRUS is inserted until its transverse image plane is viewing the apex of the prostate. The probe is mounted on a stepper mechanism that is able to withdraw the probe at 5 mm intervals. This movement is indicated by the gray arrow. Transverse images are taken at each interval until the base of the prostate is reached. The entire prostate volume is imaged in this way.

The volume study is based on a set of transverse images collected using a trans-rectal ultrasound (TRUS) probe. The TRUS probe is mounted on a holder that is attached to a stepper support structure. This stepper is able move the probe at 5 mm step intervals forwards and backwards. The patient is brought into the operating room and placed in the lithotomy position. The TRUS probe is manual inserted into the patient's rectum and the support structure is locked in place. The final position of the probe relative to the prostate is shown in Figure 2.1.

The stepper is then used to move the probe deeper into the patient's rectum until the apex

of the prostate is just visible on transverse image of the ultrasound system. The probe is then slowly withdrawn using the stepper in incremental steps. For each of these steps, a transverse ultrasound image is taken of the prostate region. This is done until the base of the prostate is reached.

The set of transverse images forms a three dimensional study of the prostate volume and specialized software is then used to analyze this image stack. Two dimensional outlines of the prostate, urethra, and rectum are visually determined on each image in the stack. The sets of contours that result create three dimensional representations of the organs.

Finally, the positions of the radioactive seeds are determined. In brachytherapy, seeds are implanted via needles and inserted into the prostate parallel to the TRUS probe. Seeds that need to be inserted at different depths but at the same position on the transverse plane are inserted using the same needle. To increase the number of seeds that can be implanted with one needle, certain constraints are applied to where the seeds can be placed.

Seeds are made to associate with specific images in the volume study and the depth of the seeds correspond to the depth of the plane of its associated image. The seed's position on the image plane is constrained by a superimposed template on the image. This image template is made to match a physical needle insertion template used during the implantation process. The needle insertion template is fixed in position relative to the TRUS probe and forces needles to be inserted parallel to the TRUS probe (directly into a transverse image planes).

The valid positions on the image template correspond to physical insertion holes on the needle template. Seeds that are in valid positions on the image template will be able to be deposited in needles going through the corresponding holes on the insertion template.

Constrained by the above factors, seeds are distributed across the volume of the prostate. A dosimetry profile is constructed from the seed positions which indicates the level of radiation delivered to different regions. Isodose contours are computed from this dose profile and are superimposed onto the organ outlines to determine the degree of radiation exposed to different organs. Manual and automated optimization procedures are then conducted on the seed positions to obtain the best dose distribution (for more detail on what it means to have the best dose distribution, consult Section 2.3).

A final written report, such as the one shown in Figure 2.2, is then created to serve as a guide in implantation process. In the report, needle insertion depth and transverse positioning are determined. The transverse positioning is given in terms of the coordinate system of the seed placement template while the depth is set based on the depth of the corresponding image planes that the seed is placed on. Details regarding the number and distribution of seeds within each needle are also given.

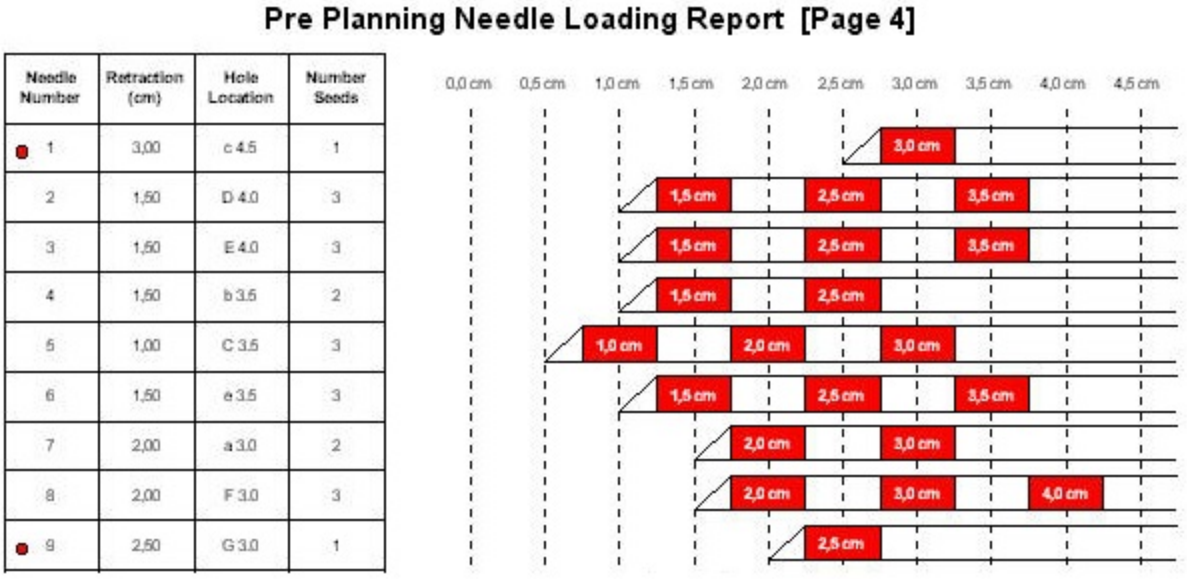

Figure 2.2: In a planning report, the table on the left has needle insertion information. Each needle is uniquely identified by a number. On the table, each needle's retraction distance is given along with its insertion location on the needle template. Note the positioning on the template is alphabetically on one axis and numerical on the other. The number of seed for each needle is also given. On the right, the distribution of seeds in each needle is illustrated.

2.3 Seed Placement and Dosimetry Considerations

I_{125} and Pd_{103} are the primary isotopes used to create brachytherapy seeds. Both radiation sources are X-ray emitters that decay via electron capture. I_{125} has a photon energy of 28 keV and Pd_{103} has an energy of 21 keV[24]. The primary difference between the isotopes is the rate of decay with I_{125} having a half-life of 60 days and Pd_{103} having a half life of 17 days[24]. However, there is no definitive evidence to suggest that one is better than the other for the purposes of brachytherapy[11].

The isotopes deliver extremely localized radiation with a rapid fall-off in energy away from the source center. Radiation measurements taken in air around an I_{125} and Pd_{103} radiation source shows more than a 90% fall-off between the doses at 5 mm and 15 mm from the source[24].

The localized nature of brachytherapy sources mean changes in their positioning can drastically change the generated dose profiles. This can cause some targeted areas to be under-dosed and others to be over-dosed. This is an important issue as the dose delivered to different areas in the target region affects the success of the procedure and the patient's quality-of-life.

The primary goal in brachytherapy is to deliver enough radiation to the cancerous tissues of the prostate to kill all proliferating cancer cells. Cancer cells that are not killed will proliferate again leading to a recurrence. Studies have indicated that the entire prostate region needs to be exposed to radiation levels of around 160 Grays in order to minimize the likelihood of cancer recurrence[20].

To guarantee adequate radiation is delivered to the cancerous tissues of the prostate, it might be tempting to distribute a set of very high dosed seeds throughout the prostate. However, high radiation exposures to the organs neighboring the prostate can damage them and create adverse and long-term complications.

The urethra runs lengthwise through the center of the prostate. High dose delivered to the urethra is associated with increased likelihood of long-term urinary morbidity[19, 22]. To avoid this, seeds are not implanted in close proximity to the urethra. This limits them to the more peripheral regions of the prostate[24].

High doses of radiation exposed to the rectal walls are associated with an increase in the risk of ulcerations and bleeding, leading to long-term rectal complications[22]. The anterior wall of the rectum is situated adjacent to the posterior side of the prostate making it difficult to deliver the necessary high doses to the periphery tissues of the prostate without exposing the same dose to the wall of the rectum[24]. Care is taken to avoid placing seeds to close to this region.

The prostate is also surrounded by neurovascular pedicles and other structures that are required for penile erectile functions. High dose exposure to these tissues can cause damages that increase the chance of impotency following the operation [18]. To avoid this, seeds are kept within the confines of the prostate volume as much as possible.

Without careful planning, delivering the necessary level of radiation to the cancerous tissues

of the prostate can negatively impact the surrounding tissue resulting in increased risk of post-operative complications. The final seed positions determined from the planning process should strike a fine balance between the goals of killing cancer tissue and sparing healthy tissue.

2.4 The Implantation Procedure

The brachytherapy seed implantation procedure is conducted using the same setup as the one for the volume study. The patient is once again placed in the lithotomy position and the TRUS is inserted into the patient's rectum.

The TRUS needs to be in the same position relative to the prostate area as it was in the plan, otherwise the clinician will not be able to correctly insert the needles as indicated by the plan.

To do this, the ultrasound system is set to actively display transverse images as the TRUS is manually inserted into the patient's rectum. The positioning of the TRUS is adjusted until it is able to roughly obtain the same image of the apex of the prostate as in the volume study. This is usually done by matching specific calcification structures and organ outlines between the planning image and the current image. The TRUS is then stepped outwards to determine the correlation of the current set images with those from the volume study. The TRUS adjustment continues until the image sets match closely.

Once the TRUS is positioned correctly, the needle insertions begin. The needles are inserted past the insertion template (through the holes at the planned grid positions), through the patient's perineum and into the patient's prostate. Since the current image plane depths are matched to the ones in the volume study, the stepper is used to obtain the transverse image at the planned insertion depth. The needle is inserted until it is just visible at this depth and the strand in the needle is then deposited.

The deposition of a strand involves pulling back the hollow cover of each needle while holding the central rod in place. Once the hollow needle no longer covers the strand, both the needle and the central rod are pulled out. This deposits the strand in the prostate.

The needle insertion process continues until all the strands are implanted into the prostate. The last step in the operation checks the quality of the implant. This involves determining the final seed placement and is usually done using a CT scanner. The scanner collects a series of cross-sectional images of the prostate region. Seeds show up as bright spots on these images while strand materials and soft tissue are harder to discern.

From these images, the seed positions are identified and dosimetry is calculated. The resulting position and dose information are then compared to the preplan in order to determine the accuracy of the seed placement and determine any areas that are under-dosed. Reconstruction from fluoroscopy images and MRI imaging are alternatives to CT in post-operative analysis[12].

2.5 Intraoperative Modification

Though brachytherapy has been shown to be a valid treatment option with relatively low post-operative complications, the traditional two step process of planning and implantation creates a great degree of uncertainty in the procedure. These uncertainties are attributed to differences in setup between the two stages of the procedure as well as errors in the seed implantation process. The actual positions of the seed that are implanted can differ greatly from where they should be as illustrated in Figure 2.3.

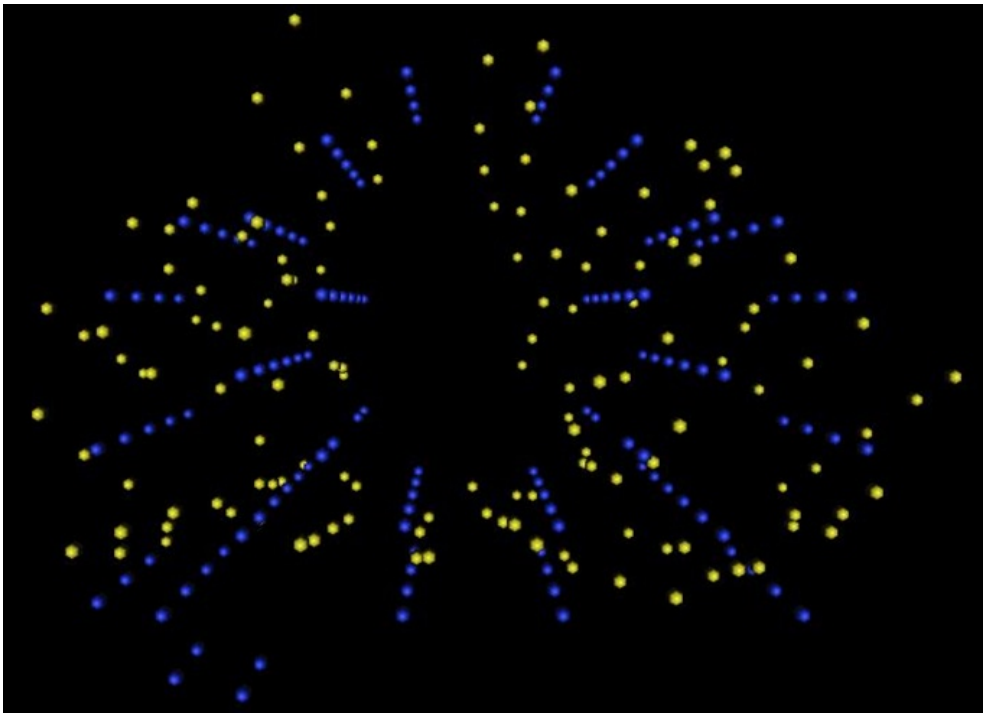

Figure 2.3: 3D reconstruction of the planned seed positions in a brachytherapy procedure (blue). This is superimposed over the actual implanted seed positions (yellow). The implanted seed positions are determined using fluoroscopy reconstruction

During the implantation stage, the clinician has to manually match the relative TRUS to prostate position to what it was in the volume study. This is a very time consuming and inaccurate process. Anesthesia applied to the patient during implantation stage can further complicate this as it relaxes the muscles around the prostate region and alters the size and shape of the prostate[24]. The prostate can also change size in the period between the volume study and implantation [13].

In addition to TRUS positioning errors, inaccuracies in strand placement can account for large seed positioning changes from the plan. Patient movement and motion due to respiration can cause errors in needle to prostate positioning. The prostate can swell due to edema and

increase in size during the course of implantation. The prostate can be deformed by the force of the inserting needle and the needle can also be bent by the force of the surrounding tissue[7, 13].

As discussed in Section 2.3, an adequate dose of radiation must be delivered to the cancerous tissues of the prostate while exposure to other functional organs surrounding the prostate should be minimized. However, the localized nature of the radiation from the brachytherapy sources mean any errors in placement can cause planned high dose areas to not receive enough radiation and planned low dose areas to receive too much radiation.

To reduce these errors in the treatment procedure, the American Brachytherapy Society recommends[13]:

> "[Striving] for on-line, real-time intraoperative dosimetry to allow for adjustment in seed placement to achieve the intended dose."

In the ideal situation described above, a dynamic treatment plan is created in real-time by heavily modifying the plan created in the planning stage. Actual implanted seed or strand positions are determined after each needle deposition. The radioactive source positions are then fed into a computer algorithm that constructs, in real-time, an accurate dosimetry profile of the prostate volume. This process is called real-time dosimetry. Based on this up-to-date dosimetry profile, new strands can be added and existing strand positions can be modified to compensate for any errors in dose delivery[13].

Current intraoperative planning procedures do not fully reach the ideals set by the American Brachytherapy Society. To reduce setup differences, some clinicians conduct the planning stage of brachytherapy immediately prior to the implant stage. In this, the same setup is used in both stages and clinicians not longer have to match up the TRUS positions. However, this puts a tight constraint on the planning process and can extend the operating time of the procedure[13]. This process is called "intra-operative preplanning".

To account for needle flexion and movement of the prostate due to needle insertion, certain procedures have tried to intraoperatively detect the path of the needle as they are inserted. In these procedures, a set of needles are inserted and then imaged by a sagittal image sweep, conducted by spinning the TRUS probe around its axis. The sweep is used to reconstruct the needle positions in three dimensional space and can be used to determine any needle insertion errors[13, 25].

The two modified brachytherapy protocols described above manages to remove some uncertainty in the procedure, but does not fully solve the problem. Even being able to localize the needles does not allow us to localize implanted strands as the seeds and strands still move during the deposition process and are often not deposited following the needle path[13].

The inability to accurately localize radioactive sources prevents the creation of accurate real-time dosimetry profiles. This, in turn, hinders the ability to detect and compensate for tissue areas that are receiving inadequate dosage.

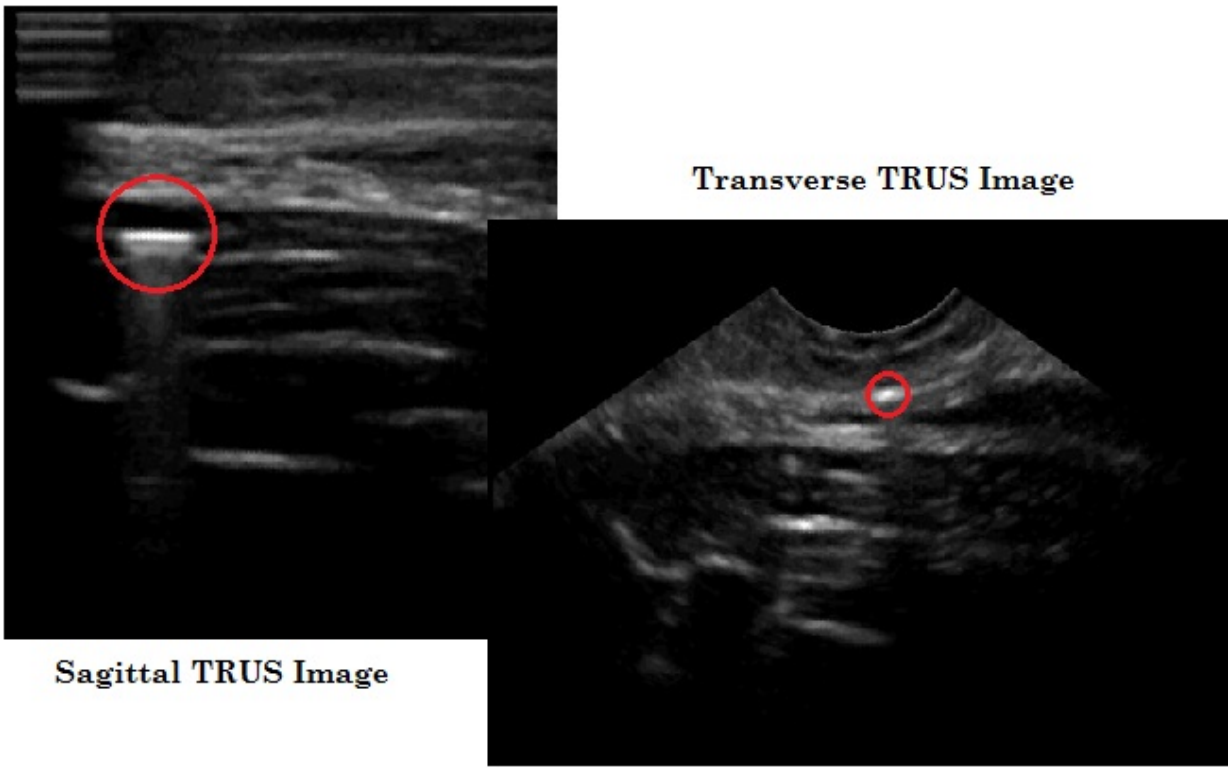

Figure 2.4: In both transverse and sagittal TRUS images, implanted brachytherapy seeds in tissue is extremely hard to discern due to the noisy environment. The implanted seed is circled in red in the images above. $DataCredit : Xu, UBCRCL$

Attempts had been made to try to localize planted seeds using the TRUS probe. Since it is already used to guide needles insertions, it is a convenient medium to use in attempting to localizing radioactive sources. However, an ultrasound image of the prostate area is extremely noisy. Numerous calcification sites, speckles and shadow artifacts are present in these images, as can be seen in Figure 2.4. Small seeds tend to show up very poorly on traditional TRUS ultrasound images [8, 23]. The strands provide a bigger profile for detection but parts of them do not generate a strong intensity response on ultrasound images (see Section 2.6).

More advanced ultrasound techniques such as Doppler Ultrasound and vibro-acoustography have been used to enhance the contrast between the seed and background noise. However, these techniques require the addition of specialized equipment making them inconvenient for a tightly scheduled procedure [8, 9].

Other than ultrasound, MRI and X-ray fluoroscopy provides excellent seed localization abilities but the extra imaging equipments impart a large overhead. The high cost associated with MRI imaging makes it hard to incorporate into brachytherapy. X-ray fluoroscopy is much cheaper but it can't visualize the prostate contours meaning that the positions of the imaged seed relative to the prostate can't be directly determined[3, 15].

2.6 Regular and EchoStrands^{TM}

Seeds loaded into brachytherapy needles come in two different forms, loose seeds and stranded seeds. Both types carry distinct benefits and drawbacks and are often used in conjunction in a single brachytherapy procedure.

Loose seeds come in a set of individual seeds with spacer materials of different length. Based on the requirements, the seeds are individually loaded into insertion needles and spaced out at specific intervals by a spacer material. Once the needle is loaded with the necessary number of seeds interspaced by the correct spacers, it is ready to be used.

Loose seeds carry the benefit of allowing new needles to be created intraoperatively with the desired number and depth of seeds. This allows for great flexibility during the operation as clinicians can active modify the plan and creates new needles that reflect the modifications.

The alternative to loose seeds is stranded seeds or strands. Strands consist of seeds sutured together along with spacers into a single long structure that is loaded into the needle as a whole. The entire strand is then deposited into the patient's prostate. The strands are often made by the manufacturer before-hand and must be ordered during the planning stage. This gives the clinician less flexibility during the procedure but makes the insertion process faster. Stranded seeds also prevent seed migration from occurring.

Seed migration occurs when loose seeds are inadvertently implanted outside the venous plexus surrounding the prostate gland causing them to be carried off by blood vessels to the pelvis and even the lung[4].

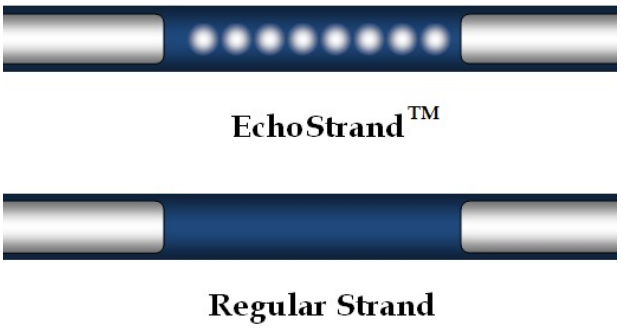

Figure 2.5: EchoStrands^{TM} (top) have small gas filled micro-bubbles within its spacer material (spacer material is shown in blue). The spacer material of a regular strand (bottom) has a uniform composition.

Traditional spacer material found in strands and with loose seeds is made from a uniform bio-absorbable suture material composed of braided Vicryl (polyglactin 910) and is thermally stiffened[24]. In strands, this material is also used to encase the seeds. This material is required to be bio-absorbable as the entire strand is permanently implanted within the prostate. The

long strands will cause long-term discomfort in patients if the spacer material holding the strand together does not degrade over time.

The bio-absorbable requirement of the strand material limits the selection of materials that make these strands. The bio-absorbable materials that are currently available show up poorly in ultrasound, making it hard to visualize entire strands accurately.

A new form of strand is now available called EchoStrand^{TM} (See Figure 2.5). The spacer materials of these EchoStrands^{TM} contain specially embedded gaseous micro-bubbles that increase the ultrasound intensity response of the strand. These micro-bubbles are filled with gas, which is generally a very poor medium for ultrasound propagation. This results in most incoming ultrasound beam being reflected at the boundaries of the gas filled micro-bubbles, making them extremely reflective.

The use of micro-bubbles as contrast agents in ultrasound has been an active point of research in recent years in the field of contrast enhanced ultrasound. This technology is used mainly in the analysis of the vasculature of large organs. The micro-bubbles in used in those experiments are enclosed volumes of gas surrounded by a shell of organic material such as albumin. They are then injected into the blood stream to be detected by the ultrasound[1, 17].

Chapter 3

Ultrasound Image Analysis

3.1 Basics of Ultrasound Imaging

In ultrasound imaging, a transducer both emits and collects sound waves through the use of its piezoelectric crystals. A piezoelectric crystal undergoes high frequency vibrations in response to electrical signals, producing ultrasound in the process. The ultrasound waves are focused into a narrow beam directed at the tissues being imaged. The sound waves exert varying pressure on the particles in the medium transmitting their energy and causing these particles to vibrate in place. The sound energy is continuously propagated by the transfer of this energy from particle to particle[21].

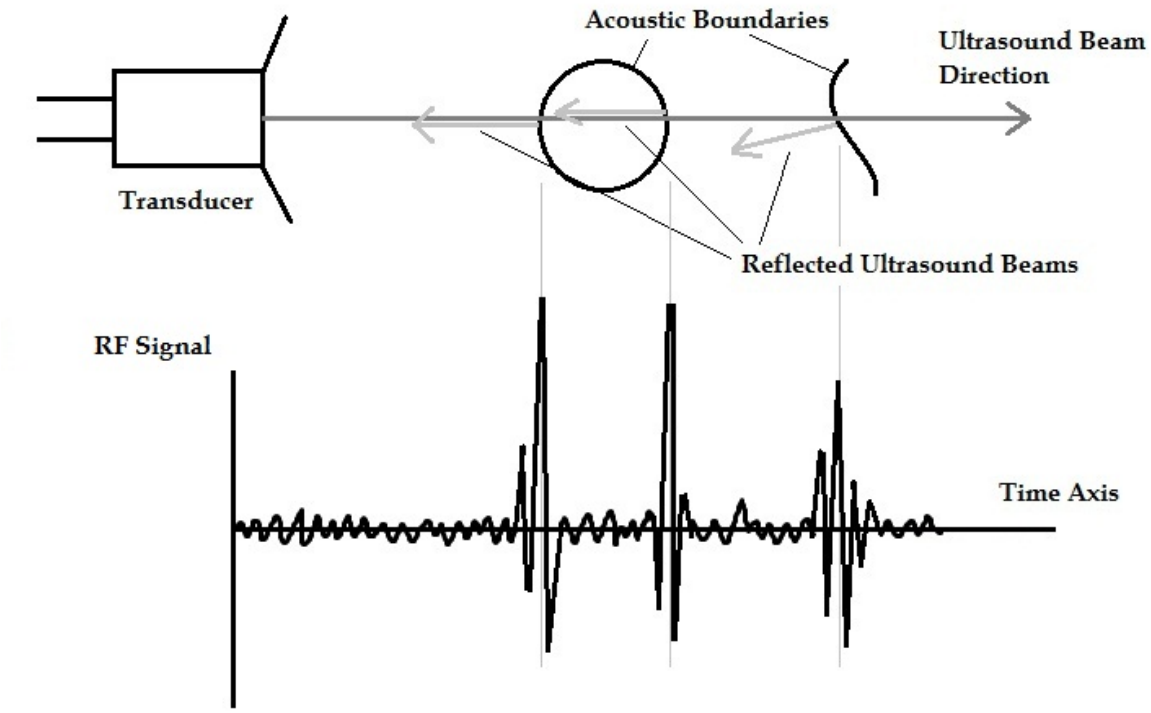

Figure 3.1: The reflected ultrasound echoes are saved in the form of a radio-frequency (RF) signal plotted on a time scale. High amplitudes on this plot correspond to reflective boundaries in the medium with the position along the plot corresponding to distance to the reflective boundary.

Emitted ultrasound energies propagate through a medium until they encounter an acoustic boundary. These boundaries form between two mediums of differing densities. At these boundaries, a portion of the ultrasound energy is reflected back as echoes which are then picked up by the original transducer. The crystals of the transducer then converts and records the received sound energies into a electrical signal (as shown in Figure 3.1)[21].

The total strength of the echoes received at a specific time is recorded as a time-based radiofrequency (RF) signal. Since echoes from greater depths take longer to travel back to the transducer, received echo time is directly proportional to the depth of the echo's corresponding reflective boundary[21].

Each piezoelectric crystal is designed to project ultrasound in a narrow beam, detecting reflective boundaries at various depths along a single direction. The transducer uses a linear array of these crystals to collect data on a plane[21]. There are typically two sets of these arrays on a TRUS probe, allowing it to collect both transverse and sagittal images (See Figure 3.2).

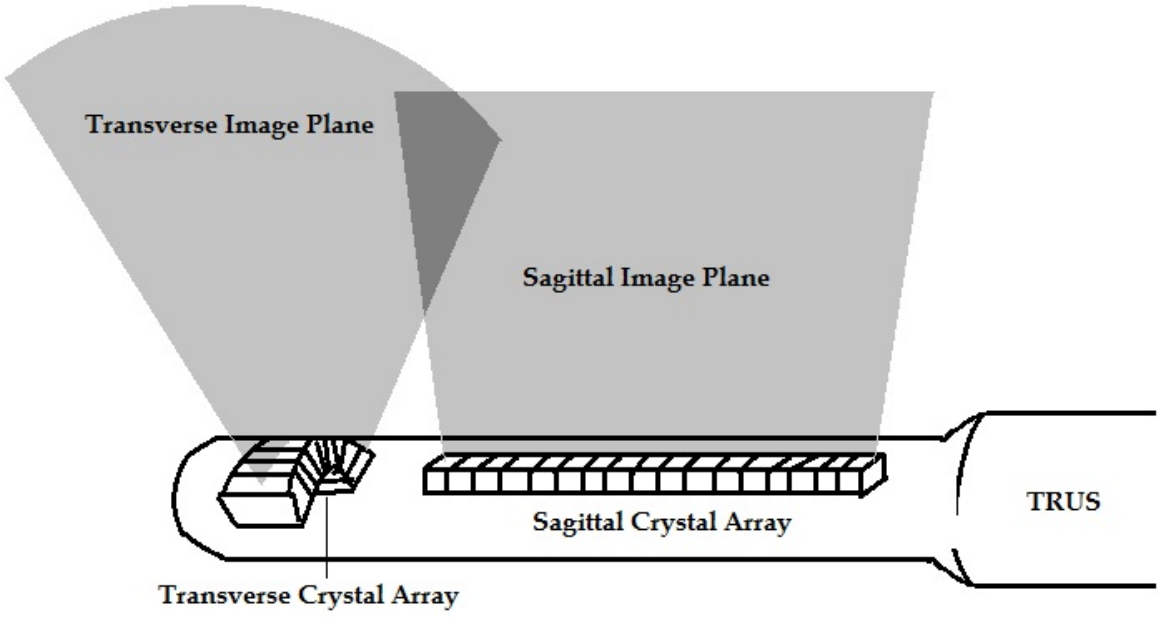

Figure 3.2: The TRUS probe can image two image planes. The transverse image plane is generated by data collection from a crystal array that runs radially around the tip of the TRUS. The sagittal image plane is generated by a crystal array running along the length of the TRUS.

The final ultrasound image is composed from a set vertical scan-lines. Each scan-line corresponds to the RF signal generated by one of the crystals in the array. The pixel intensities along each scan-line are relative to the RF signal strength received from echoes at specific depths.

The raw RF signal varies over an extremely large range. In order to fit it into a displayable

pixel value, the RF intensity is first filtered and compressed to be within the intensity range of normal tissue. The output image is the familiar B-Mode ultrasound image.

3.2 Image-Based Strand Localization Considerations

The goal of this project is to determine how well our methods work at localizing implanted brachytherapy strands in three dimensional space.

Strands can be localized on image planes by determining its position on the image. However, when there is an image stack and the strand appears on several images in this stack, it is important to determine on which image plane the strand corresponds to. This is discussed in Section 3.2.1.

The orientation of the strand is also expected to influence the ability to localize these strands. The interaction between ultrasound image intensity responses and the strand orientation is discussed in Section 3.2.2.

3.2.1 Localizing to Image Planes

In order to localize the implanted strands using ultrasound, its positioning needs to be accurately determined across all axis in three dimensional space. However, ultrasound images are in two dimensions and in order to reconstruct a three dimensional region of interest using them, a series of consecutive ultrasound image slices must be taken.

In brachytherapy, these image slices are collected by setting the TRUS probe to image sagittally. The probe then rotates around its axis (shown in Figure 3.3) collecting an image after a certain degree of rotation. The image set can then be used to reconstruct a sector volume representation of the imaged region.

Each of these ultrasound images correspond to an image plane with known positioning relative to the TRUS. Both the specific image plane that the strand corresponds to and its positioning on that image plane needs to be determined before it can be localized in three dimensional space.

The position of the strand on the image plane can be determined simply by manually or automatically segmenting the strand from the background based on its intensity response. Determining which image plane the strand corresponds to is more difficult.

During its travels through the medium, individual ultrasound beams tend to be deflected by different the particles within the medium. This means that the emitted ultrasound beams will be deflected in different directions and the transducer receives incoming ultrasound reflections sources that are not directly on the imaging plane[21]. In terms of strand localization, this results in strand that do not directly lie on the image plane still giving an intensity response.

Fortunately, the intensity responses of strands that are not directly on the image plane are weaker than those from strands that are. In addition, the further away the strand becomes from the imaging plane, the weaker its response becomes. This property allows the determination of the corresponding image plane of a strand with a degree of uncertainty.

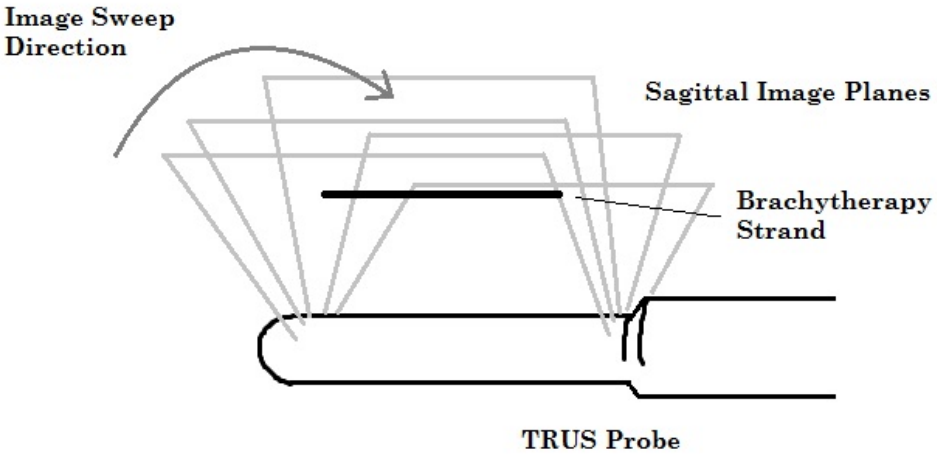

Figure 3.3: The strand positioning can be determined by collecting a set of sagittal images as the TRUS is rotated around its axis. The set of images can then be used to reconstruct the sector volume around the strand. However, one major issue is determining which image plane the strand is actually on.

For the purpose of localization, it is desirable to receive a large intensity response when the strand is directly on the imaging plane and a rapid falloff in intensity as the strand is further away from the imaging plane. Once this intensity response versus distance to imaging plane is known, strands that are on the imaging plane and strands not on the plane can be separated. A threshold value can be set such that the strand with intensity above the threshold is associated with the image plane while those below belong to another image plane. With a rapid falloff of intensity, we can more accurately make this distinction taking into account natural variation in strand intensity.

In the situation where the strand intensity response does not have a rapid falloff, it becomes much harder to separate between strands that are close to the image plane and those that are far away. A greater degree of uncertainty is associated with strand positions in this case.

There will always be a degree of uncertainty when trying to associate an intensity response to a particular image plane. However, large drop-offs in intensity as the strand moves away from the imaging plane makes it easier to do so.

3.2.2 Effects of Strand Orientation on Ultrasound Reflectance

One of the major sources of error in seed and strand placement is needle flexion. As the needle is inserted into the patient's body, it is deflected through the interaction of the surrounding tissue with the tapered needle tip. When such a needle then deposits its strand, the strand is deposited in a bent shape and at an angled orientation[2].

Imaging both seeds and strands on ultrasound at different orientations will give different intensity responses. This has to do with how ultrasound reflection is generated on these strands. There are two types of reflection in ultrasound. Specular reflection occurs with a relatively large and smooth acoustic boundary while non-specular reflection occurs with a smaller and irregular boundary.

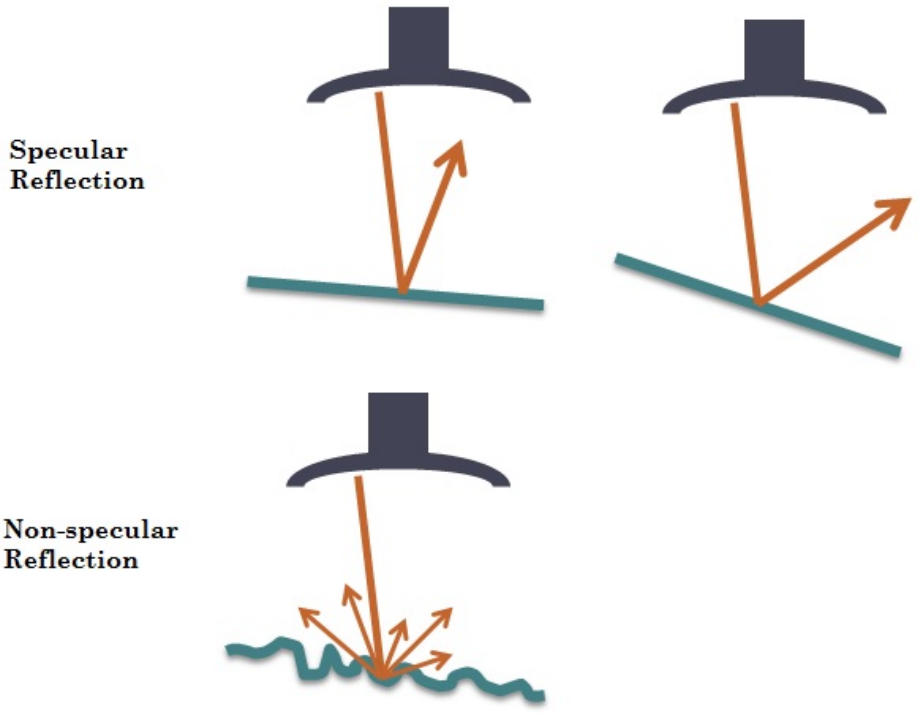

Figure 3.4: In specular reflection (top), the incoming ultrasound beams are reflected from the surface in a very uniform manner. This occurs on smooth reflective boundaries. In non-specular reflection (bottom), the incoming ultrasound beam is scattered in all directions when in contact with an uneven reflective boundary

A simple law governs specular reflection. The direction of the reflected ultrasound beam is on the opposite side of the normal in relation to the incident beam with the angle of incidence equal to the angle of reflection[21]. Based on this, the chance of the transducer that emitted the ultrasound beam receiving its echo is expected to be higher as the angle of incidence and reflection decreases. When the beam incident ultrasound beam is perpendicular to the surface of the boundary, it is expected that the echo will go straight back to the transducer. This is illustrated in Figure 3.4.

Non-specular reflections or scattering does not obey any simple laws of reflection. The rough surfaces that cause non-specular reflections reflect ultrasound beams back in many different directions. These reflections tend to be much weaker than specular ones but are not affected by

changes to the surface orientations as illustrated in Figure 3.4.

Ultrasound seeds are long cylindrical objects. The length of each seed is much greater than the diameter of its cross-sectional area. This meaning most incoming ultrasound beams hit along its lengthwise surface. These surfaces are extremely smooth resulting in mostly specular reflections.

When we change the orientation of the seed, we change the orientation of the seed's lengthwise surface. A very high intensity response is expected for seeds orientated with its length perpendicular to the incoming ultrasound beam as the ultrasound beams are echoed back in the direction of their origin. The intensity is expected to decrease as the seed is orientated in away from this angle which directs ultrasound echoes away from their source. This effect is seen in B-Mode images as well as in average-reflected-power images [2]. Figure 3.5 illustrate the effect in the later image type.

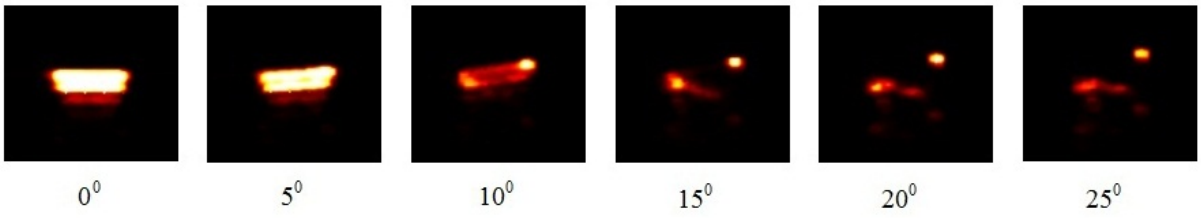

Figure 3.5: A set of average-reflected-power images of brachytherapy seeds of different orientations implanted in a phantom. The intensity of the cylindrical implanted seed is seen to decrease as they are orientated to steeper angles. $DataCredit : Xu, UBCRCL$

In this experiment, the investigation is conducted on strands and not seeds. Though the composition of the strand is different than that of the seed, the overall geometry of the strand is still the same. The strands are still cylindrical with most of ultrasound reflectance occurring along its lengthwise surface. It is expected that the same intensity falloff will also occur in strands as it was seen for seeds.

This means that any intensity response or contrast analysis on the strands needs to be done over a range of different orientations to account for the intensity falloff.

3.3 Average-Reflected-Power Imaging

A lot of contrast is lost when the A-lines signals are converted into B-line intensity dots. To overcome this problem, the average-reflected-power imaging technique used in this project directly generates high contrast images from the information in the A-lines without any form of compression.

This technique is developed by Xu Wen at the UBC Robotics and Control Laboratory and has been used in previous studies to better localize implanted brachytherapy seeds. The imaging

technique was found to greatly enhance the intensity response of the seeds and increase their contrast over background noise, resulting in better localization[23].

In this imaging technique, the A-line is first divided into a number of overlapping blocks. For each of these blocks, the amplitude of each of discrete signal value in these blocks are averaged to generate a single average intensity response. This averaging can be done over both the time domain and the frequency domain. This process is illustrated in Figure 3.6.

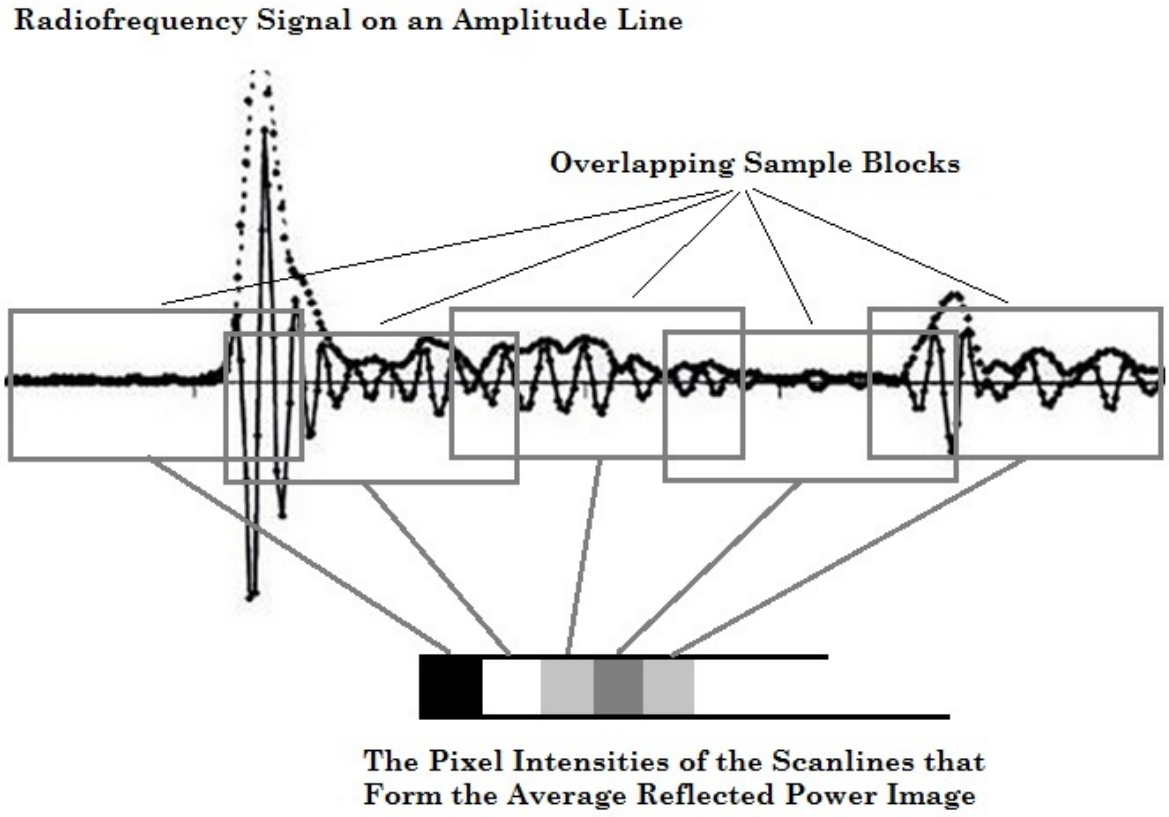

Figure 3.6: In average-reflected-power imaging, the amplitude line is divided up into short overlapping blocks. The intensity within each of these blocks is averaged over the time domain or the frequency domain. The averaged value for each amplitude line then forms a scan-line in the average-reflected-power image.

The calculation of the average over the time domain is conducted in a relatively straightforward manner. Within each block, the squared modulus of the discrete intensities of the RF signal is averaged using Equation 3.1. The average intensity for the block at depth d, indicated by $P_A(d)$, is calculated from the discrete intensity signal values found at the different positions, k, along the block indicated by $x_d(k)$.

$$P_A(d) = \frac{\sum_{k=0}^{N} |x_d(k)|^2}{n} \tag{3.1}$$

Parseval's Relation states that the total energy in an n-point frequency spectrum of a signal is equal to its total energy in the n-point time sequence[14]. Following this relation, as illustrated in Equation 3.2, the average intensity for the block can also be calculated over the frequency domain.

$$\sum_{n=0}^{N-1} |x[n]|^2 = \frac{1}{N} \sum_{k=0}^{N-1} |X[k]|^2 \tag{3.2}$$

To average the block of signal over the frequency domain, the signal in each block has to be first converted into the frequency domain. Fast Fourier Transform (FFT) is used to convert the original signal into a Fourier spectrum which is a representation of which frequencies are present in the original signal.

However, the Fourier Transform tend to give a non-zero responses for frequencies close to the true signal frequency. These "spectral leakages" will interfere with the signal averaging process. To prevent spectral leakage, the Hamming Window, given in Equation 3.3, is first multiplied to the signal. This window function serves to minimize the nearest frequency responses to the actual signal frequencies. This reduces spectral leakage in the resulting Fourier spectrum.

$$w(n) = 0.54 - 0.46cos(\frac{2\pi n}{N-1}) \tag{3.3}$$

The squared modulus of the Fourier Spectrum is then averaged using Equation 3.4, where $P_d(f_k)$ is the squared modulus of the magnitude of the k'th frequency component in the 2N-point power spectrum of the segment. Only N points are used since the spectrum is symmetric about half of the sampling frequencies. These values are summed to calculate the averaged intensity value at depth d.

$$P_A(d) = \frac{\sum_{k=0}^{N} P_d(f_k)}{(N+1)^2} \tag{3.4}$$

Although calculations in both domains can give equivalent results, the computation in the time domain is much faster since it does not involve FFT. Average over the frequency domain allows the sub-sampling of intensity responses over a set range of frequencies. This allows the removal of high and low frequency noise.

Preliminary tests performed on sets of imaged strands found no improvements in data clarity or signal to background contrast when the frequency range was limited using the frequency domain method. This is attributed to the fact that the radio-frequency intensities of the background noise is much lower than that of the strand. The removal of these noise has little impact on the final data. As a result, the average-reflected-power calculations will only be done in the time domain

for this experiment to take advantage of the much shorter computation time.

Chapter 4

Quantitative Strand Intensity Response Measurements

4.1 Experiment Methods

The first part of this experiment aims to quantitatively compare the average-reflected-power image intensity responses from both EchoStrands^{TM} and regular strands under a variety of different strand orientations and distances to the ultrasound image plane. The quantitative results from this allow the determination of the effects of strand orientation on strand image intensities as well as the ability to attribute a strand to a specific image plane. This requires the ability to both rotate the strand into different orientations and rotate the trans-rectal ultrasound probe (TRUS) so that its image plane sweepes across the strand.

The experiment is done on both types of brachytherapy strands. The regular strand is tested first, followed by the EchoStrand^{TM}. Both strands are equal in size with a cross-sectional diameter of 0.86 mm and a length of 30 mm. Both strands consistes of 3 seeds of length 4 mm. Two are situated at either ends of the strand while the third is placed in the middle. These are separated by spacer materials of length 15 mm.

An Ultrasonix 500 RP PC-based ultrasound system with a biplane TRUS transducer is used in this experiment (shown in Figure 4.1). The system allows the simultaneous collection of both B-Mode image and raw radio-frequency (RF) data.

An acoustically transparent environment with very little background noise is required for accurate quantification of the strand measurements. This is achieved by submerging both the imaged strand and the ultrasound transducer in a large bucket filled with water. Water is a very conducive medium allowing ultrasound beams to traverse through with minimal scattering, producing a silent background.

The strand is suspended in water by a specially designed strand holder. The holder, which is shown in Figure 4.2, is made from three flat pieces of stainless steel. The largest piece consists of three arms. The two smaller pieces served to wedge the ends of the strand between themselves and two of the arms of the larger piece. This suspends the strand between the two arms preventing any impedance to the incoming ultrasound beams. The three pieces of metal are held together by nuts and bolts.

To suspend the strand holder in water and also allow the strand to change orientations, the

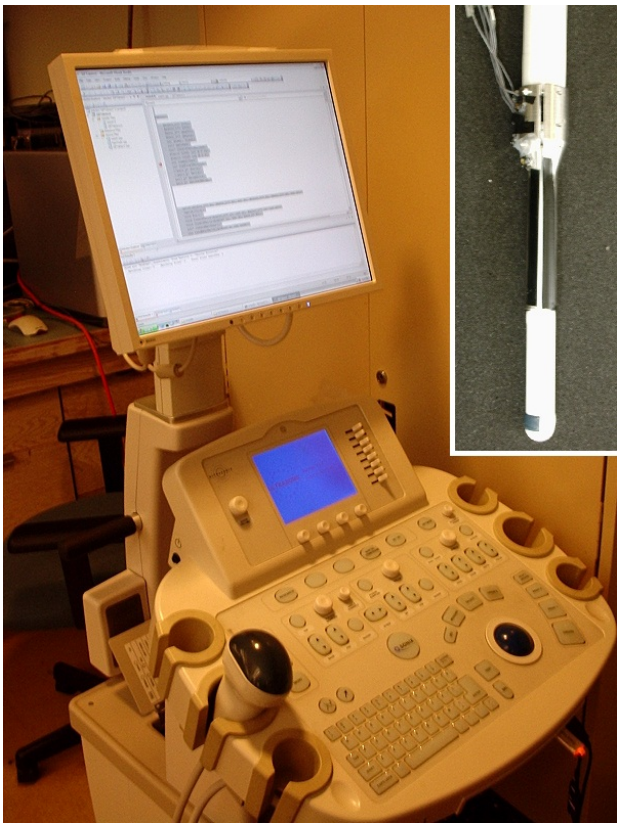

Figure 4.1: The Ultarasonix 500 RP PC-based ultrasound system with an Ultrasonix biplane TRUS transducer(inset).

last arm of the holder is attached to a large metal scaffold.

This scaffold has a U-shaped structure with a short horizontal piece that attaches to two long vertical arms. It is constructed from a long, thin piece of metal and, when folded, has a width of 7.5 cm. Each arm is 27.5 cm in length and the central portion is 16 cm long.

One of the arms is the attachment site of the strand holder and is submerged in water while the horizontal center piece of the scaffold straddles over the side of the water container. The other arm is just outside container and attaches to an upright Parker Automation M100000 Rotary Positioning Stage clamped to laboratory bench. The scaffold ensures that when the rotary positioning stage is rotated over a certain degree, the strand holder is also rotated over the same range. The position of the strand holder along the arm of the scaffold is calibrated such that the axis of rotation of the strand on the strand holder is the same as that of the rotary positioning stage. The entire setup is shown in Figure 4.2.

The trans-rectal ultrasound probe (TRUS) is mounted on a specially designed cradle system that attaches to a motorized encoder. The encoder is able to rotate the cradle around its axis and detect the degree of this rotation. Both the cradle and the encoder are mounted onto a

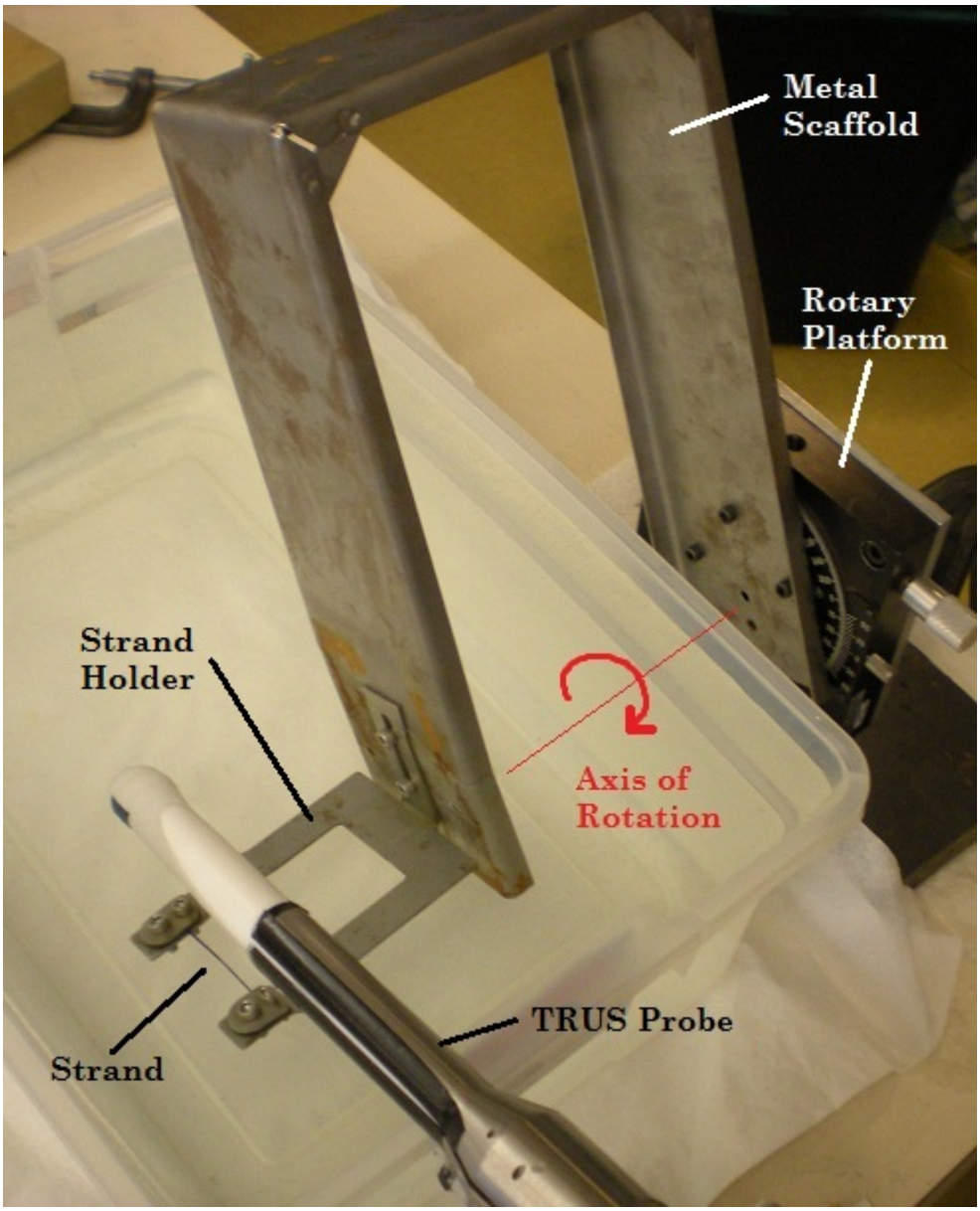

Figure 4.2: The strand holder is attached to a large metal scaffold. The holder and one arm of the scaffold are submerged in water while the crosspiece straddles over the side of the water container. The other arm is outside the container and is attached to an upright rotary platform. When the platform is rotated, the scaffold is also rotated, causing the strand holder with the strand to rotate as well. The axis of rotation of the strand is made to match that of the rotary stage (red line).

brachy-therapy platform which attaches to the laboratory bench. The basic setup is shown in Figure 4.3.

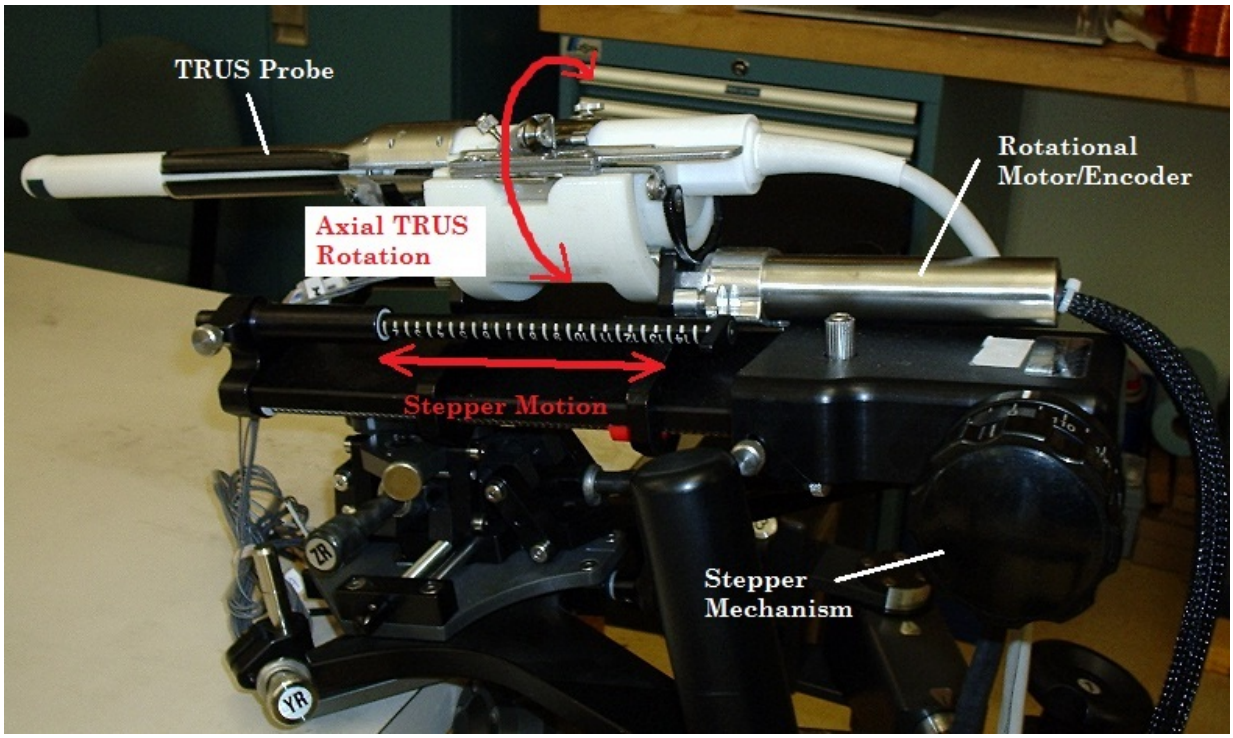

Figure 4.3: The TRUS probe is mounted on a specially designed cradle system attached to a motorized encoder device. The encoder is able to rotate the cradle and the probe around their axis. Both the cradle and the encoder are mounted onto a platform that is fixed to a bench.

The platform is then manually adjusted to place the TRUS at an angle, submerging the imaging portions of the device in the water container while maintaining the cradle, encoder and the platform over the water surface. The TRUS is positioned so that it is roughly right on top of the strand. Precision translational and rotational controls built into the platform are then used to adjust the transducer such that the transducer's incident beam directly hit the entire length of the strand. The final position of the TRUS is illustrated by Figure 4.4.

To begin the experiment, the strand is oriented to be perpendicular to the direction of the incoming ultrasound beam. This is done by rotating the rotary positioning stage until the strand appears horizontal on the output ultrasound image. This results in the long axis of the TRUS being parallel to the strand and is set to be the zero degree strand orientation angle.

The image plane from the TRUS probe is made to sweep across the strand by rotating the TRUS along its axis. Zero degree for the sweep angle is set to be when the ultrasound beam directly hit the strand. The TRUS is rotated to sweep its beam from -20 degrees to 20 degree. Custom designed software controls this rotational process and collects a series of B-Mode and

radio-frequency images. These image series are then saved to file. The angle of rotation of the TRUS is encoded into the header of the corresponding image in the file.

After the initial TRUS probe sweep at zero strand orientation, the strand is reoriented to 2 degrees. This is done by rotating the rotary positioning platform 2 degrees counter-clockwise. The same sweep procedure is repeated for this new strand orientation. In total, 12 orientations are tested at every 2 degrees from 0 to 22 degrees.

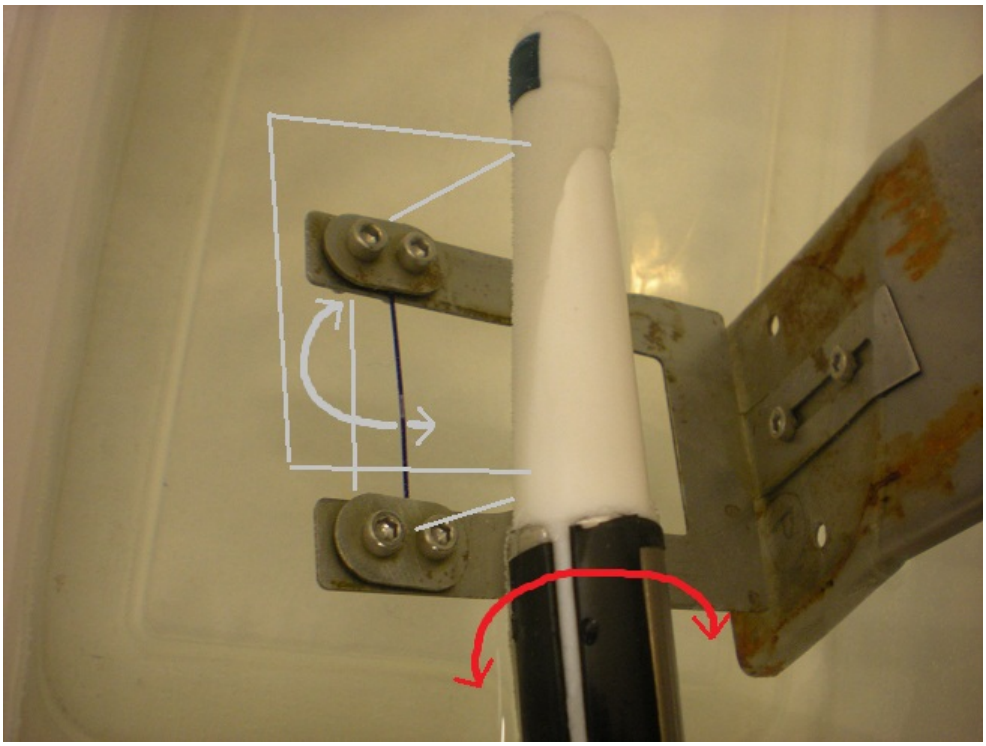

Figure 4.4: To image the strands, the tip of the TRUS is submerged in water and positioned right on top of the strand. The sagittal image plane directly intersects the length of the imaged strand. When the TRUS is rotated along its axis (red arrow), the sagittal image plane is swept across the strand (white arrow)

4.2 Image Analysis

The raw RF sagittal image data are first converted to average-reflected-power image data before the analysis took place. Each of the raw RF images compose of 176 scan-lines with length of 5696 pixels. The raw RF A-lines are split into a series of overlapping blocks. These blocks have a length of approximately 0.4 mm (137 blocks) with approximately 80% overlap. The output average-reflected-power images are reduced to 176 scan-lines with length of 80 pixels.

To account for both the intensity of the strands and the small variations in intensity along

the strand, a series of 10 rectangular regions of interests are taken consecutively along the length of the strand material (shown in Figure 4.5). These ROIs are made sure to only sample intensity responses from the strand spacer material and not from the seeds in the strands. The ROIs are 6 pixels wide and 8 pixels high which correspond to a sample dimension of 0.9 mm by 3.2 mm.

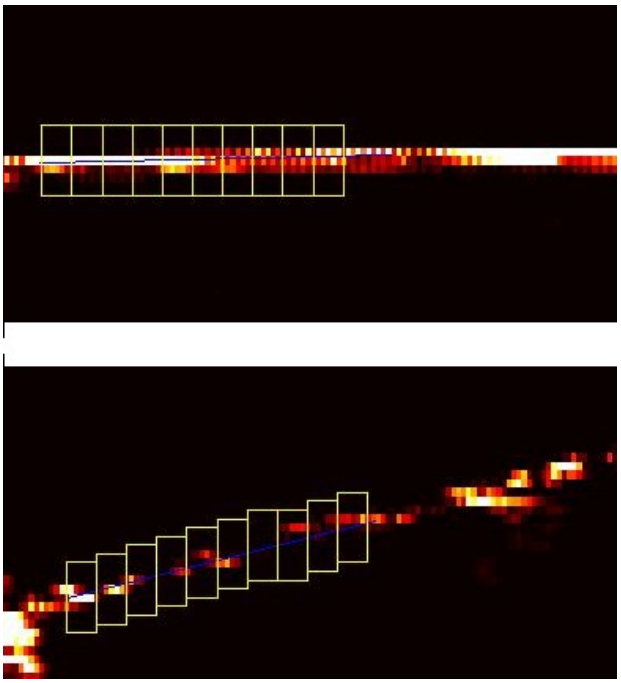

Figure 4.5: The intensity response of a strand in an ultrasound image is sampled by creating ten ROI along the length of the strand. An integral of intensity is then calculated for each sample. The above image shows the sampling for the regular strand in zero orientation (top) and fourteen degree orientation (bottom) with the set of ROIs represented by yellow rectangles.

The height of the ROIs is made to be roughly two times the width of the actual brachytherapy strand. This serves to compensate for minor changes in distance between the ultrasound source and the strand as the TRUS probe is rotated. The increased height allows the strand to be in the set of ROIs at all times during the TRUS sweep.

The integrated optical density (IOD) for each of these ROIs is then computed. This is done by summing up all the intensities of the pixels in each ROI. The mean and standard deviation of the set of IOD values from all ten ROIs are calculated giving the desired quantitative measurement of strand intensity.

4.3 Results

To analyze the intensity response of the strand in terms of their distance to the ultrasound image plane, the intensity response of the strand is plotted against the angle of the TRUS roll. Separate

plots are done for TRUS image plane sweeps for all the different strand orientations. These are shown in Figure 4.6 and 4.7.

From the plots, both regular and EchoStrand^{TM} give similar intensity profiles at low seed orientations. Both give a high intensity response when the strand lies directly on the ultrasound image plane with a rapid fall in intensity as the image plane moved away from the strand.

At high orientations, however, the EchoStrand^{TM} still maintains a sharp intensity falloff profile, but the regular strands flattens out. At these orientations, the initial intensity response of the regular strand when the ultrasound beam is incident on the strand is low and there is a much shallower intensity falloff as the ultrasound beam moves away from the strand.

To observe the relationship between strand intensity response and the orientation of the strand, images of the strand at all different orientations needs to be analyzed. We want to select from the beam sweeps the image the corresponds to when the strand is directly on the image plane. This is the image that corresponds to the peak of the beam sweep profile which occurs at the zero degree sweep angle.

The set strand images at zero degree sweep angle for both regular and EchoStrand^{TM} at different orientations are shown in Figure 4.8 in B-Mode and in Figure 4.9 in average-reflected-power.

Visual inspection of the B-Mode images indicates that the intensity responses of both strand types are roughly equivalent at low angled orientations. As the strand orientation angle increases however, the intensity and contiguity of the regular strand rapidly decreases. The EchoStrand^{TM}, on the other hand, experiences decrease in intensity but maintains its relative contiguity.

The average-reflected-power images follow the same general trend of the B-Mode. The contiguity and intensity for the regular strand decreases at a greater rate than the EchoStrand^{TM} as the strand orientation angle increases. Note that a greater range of intensity difference can be seen in the average-reflected-power images than in the B-Mode images.

The measurements of the IOD of ROIs along strands on these images are shown in Figure 4.10. The quantitative data supports our visual conclusion. The intensity of the strand falls off rapidly as the angle of the strand orientation increases. Overall, the EchoStrand^{TM} gives a better intensity response than the regular strand, though not to a statistically significant degree.

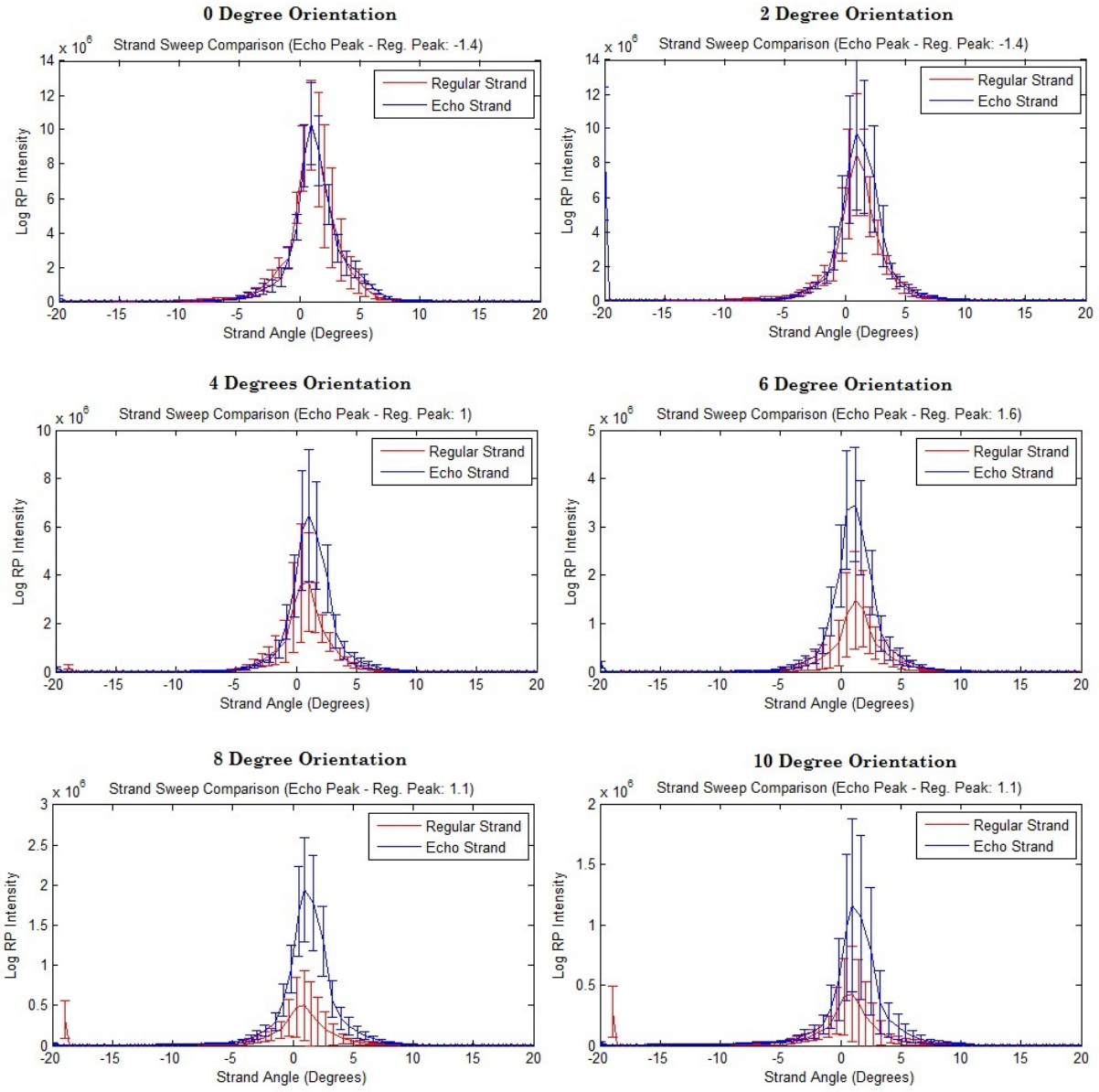

Figure 4.6: Data analyzed for strands in average-reflected-power images. The plots for the mean of integrated optical density (IOD) of ROIs along the length of the strand versus the angle of the beam sweep for strand orientations 0 degrees to 10 degrees. The TRUS is rolled from -20 degrees to 20 degrees across the strand. Its sagittal image plane directly hits the strand at 0 degrees. Overall, the strand gives the strongest responses at zero degree roll angle, when the strand is directly on the image plane. As the image plane is oriented away from the strand, the intensity response falls off.

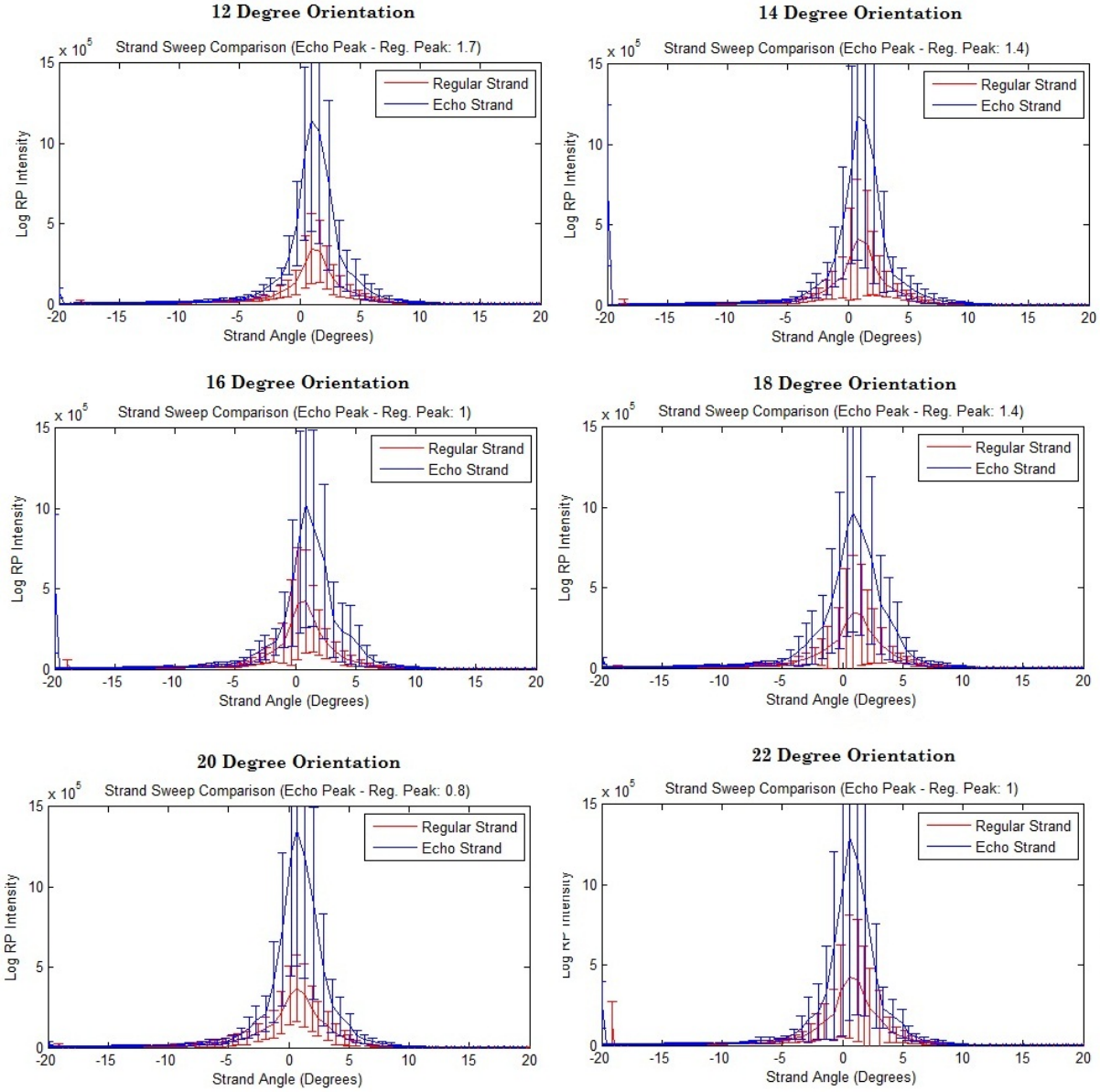

Figure 4.7: The plots for the mean of integrated optical density (IOD) of ROIs along the length of the strand versus the angle of the beam sweep for strand orientations 12 degrees to 22 degrees. The TRUS is rolled from -20 degrees to 20 degrees across the strand. Its sagittal image plane directly hits the strand at 0 degrees. Overall, the strand gives the strongest responses at zero degree roll angle, when the strand is directly on the image plane. As the image plane is oriented away from the strand, the intensity response falls off.

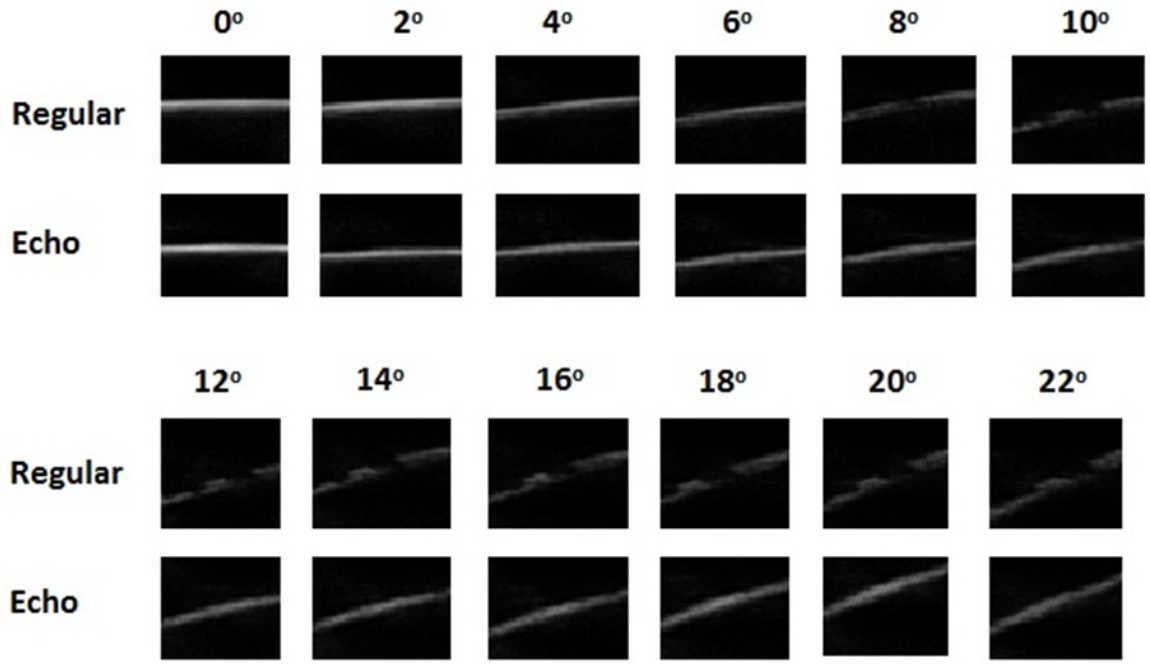

Figure 4.8: B-Mode images of short strand segments orientated at the indicated angles

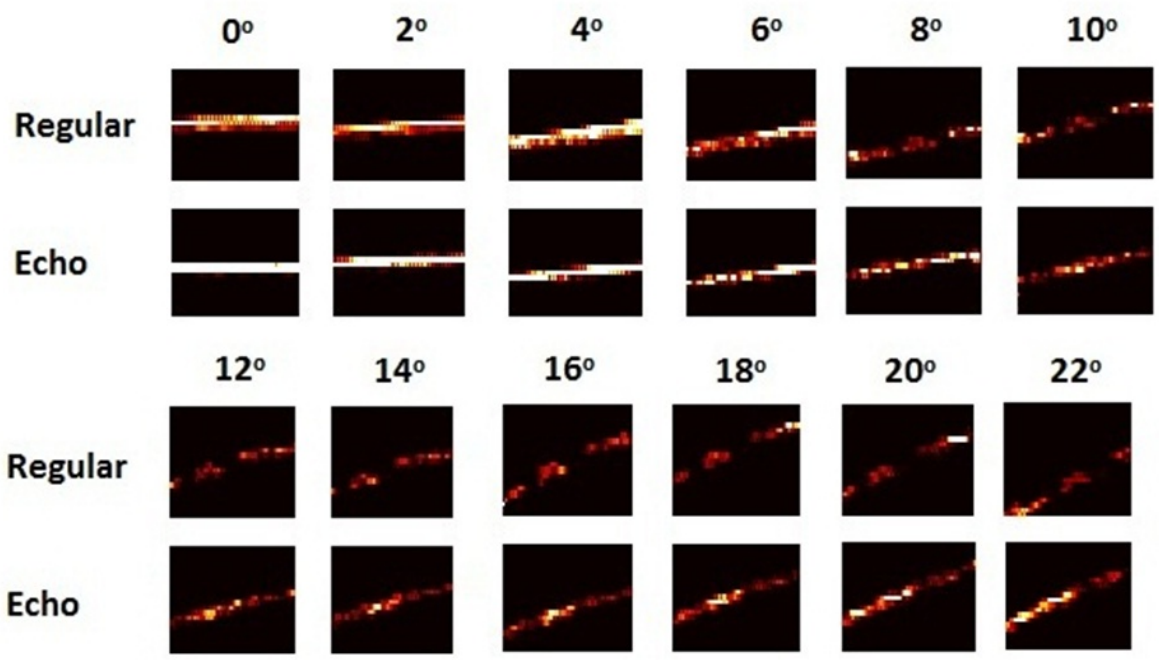

Figure 4.9: Average-reflected-power images of short strand segments orientated at the indicated angles

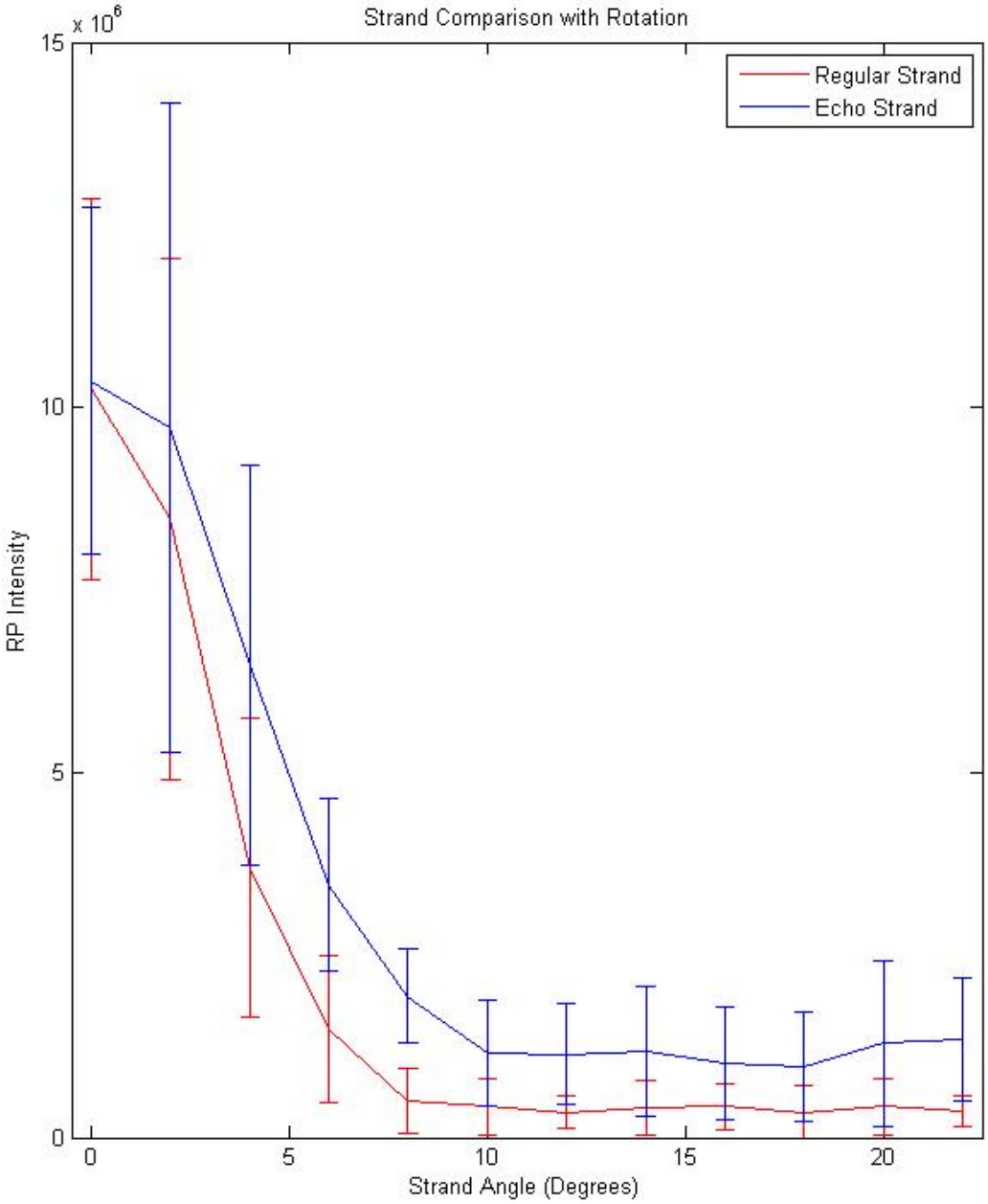

Figure 4.10: Average-reflected-power means of integrated optical density (IOD) of ROIs along the length of the strand are plotted against the strand orientation. The image being sampled is the one that gives the peak intensity output in the beam sweep which corresponds to when the strand that is directly on the plane of the TRUS sagittal image.

Chapter 5

Contrast to Noise Analysis

5.1 Experiment Methods

The second part of the experiment aims to directly compare the effectiveness of the average-reflected-power imaging in contrasting both the regular and EchoStrands^{TM} against background noise over traditional B-Mode ultrasound imaging.

A cellulose phantom is constructed in order to create a noisy medium simulating real tissue. The phantom has a rough dimension of 5 cm by 12 cm with a depth of 1.5 cm. The composition and their relative proportions are shown in Figure 5.1. Of the ingredients involved, the agar, gelatin and glycerol serve to hold the structure of the phantom while the bleach prevents bacteria from growing on the phantom. The cellulose particles are suspended within the phantom mixture, creating the noise on the ultrasound image.

Phantom Construction	
Phantom material needed for a 100g	
Agar	1.17g
Gelatin	3.6g
Cellulose	3g
Glycerol	4g
Bleach	0.25g
Water	87.98g

Figure 5.1: Relative proportions of materials needed to create 100 g of the cellulose phantom material used in this experiment.

The phantom components are combined in a beaker which is heated on a hot pad and constantly stirred with a magnetic stirring strip. Once the mixture reaches 90^oC, it is then allowed to cool while still being stirred.

When the mixture is cooled to 40^oC, half of the mixture is then poured out slowly into a small plastic box. This box serves as the mold for the phantom. The box is put into the fridge for 10 minutes allowing the mixture inside to cool and solidify. The half of the mixture that is

still in left the beaker is kept to a constant 40^oC temperature by the heating pad.

After the phantom material in the box solidifies, it is removed from the fridge. An EchoStrand^{TM} and a regular strand are placed on the solidified surface of the phantom at opposite ends. The remaining mixture in the beaker is then poured into the box completely submerging the strands and embedding them in the center of the phantom. The phantom is then cut in two to create two phantoms with a single strand in each.

Embedding the strand in this manner causes the phantom to be formed around the strand. This prevents any air bubbles from being trapped inside the phantom which might occur if the strand is inserted using needles. Air bubbles interfere gives extremely intense intensity responses and impede our ability to accurately measure the intensity responses of the strands.

The setup for this part of the experiment, shown in Figure 5.2 is very similar to the first. The same ultrasound system, transducer and strands used in the first part of the experiment are used once more. The head of the TRUS and the phantom is submerged in water to allow ultrasound beam to travel unimpeded from the transducer to the phantom.

Instead of suspending the strand in water, however, the entire phantom is mounted on a metal platform which is then attached to the same scaffold used in the first experiment. The platform performs the same role as the strand holder. When the rotary platform on the other arm of the scaffold rotates to a certain degree, the platform is also rotated. This adjusts the phantom and the strand inside to a new orientation. This action is illustrated in Figure 5.2.

The trans-rectal ultrasound probe (TRUS) is manually positioned to be right on top of the strand. Precision translational and rotational controls built into the platform are then used to adjust the positioning of the transducer such that the entire length of the strand is incident to the transducer's image plane.

To begin the experiment, the phantom and the strand inside are oriented such that they are perpendicular to the direction of the incoming ultrasound beam. This is done using the rotary positioning stage. This sets the long axis of the TRUS to be parallel to the strand and is defined again as the zero orientation angle. No image plane sweep is conducted for this part of the experiment. Instead, the TRUS simply collects a single frame of both B-Mode and raw radio-frequency (RF) sagittal data.

Once the images are collected, the strand is reoriented to 2 degrees orientation by rotating the rotary positioning platform counter-clockwise. New B-Mode and RF sagittal images are taken at this orientation. This is done for strand orientations 0, 2, 4, 6, 8, 10, 12, 15 and 20 degrees. Fewer orientations are sampled in this part of the experiment as the results from the first part indicates very little intensity response change between 15 and 20 degrees orientations.

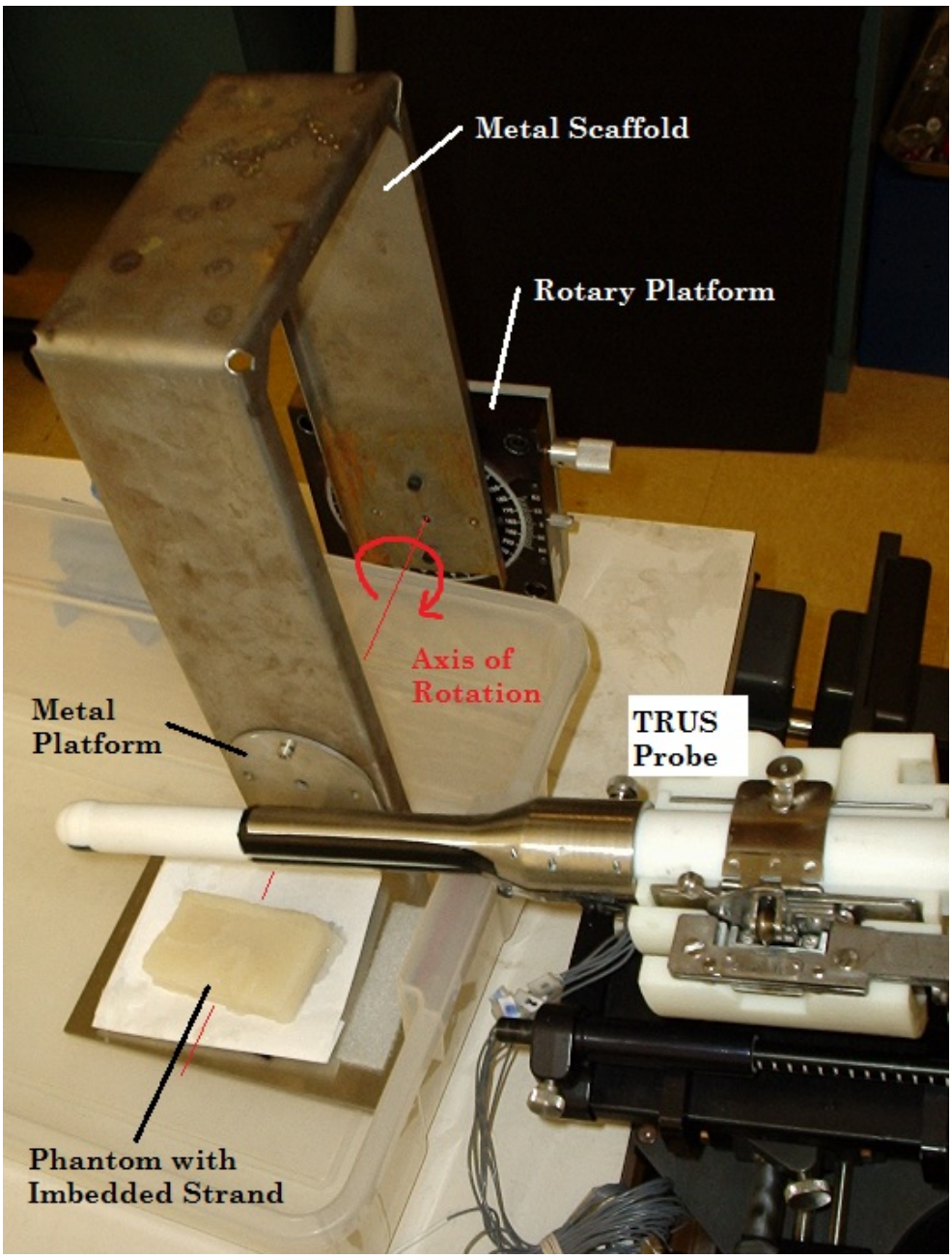

Figure 5.2: In this experiment, the phantom is placed on a metal platform that is attached to a metal scaffold which is attached to a rotary platform. Rotating the rotary platform causes the phantom and the strand inside to change their orientation. The axis of rotation of the phantom and the rotary platform is made to line up. The TRUS probe is placed right on top of the phantom in order to image the strand inside.

5.2 Image Analysis

Similar to the first part of the experiment, raw radio-frequency sagittal image data are converted to average-reflected-image data. The radio-frequency A-lines are split into a series of overlapping blocks with length of approximately 0.4 mm (137 RF samples) with approximately 80% overlap.

A certain level of contrast must exist in order to successfully distinguish the strand from background noise. A quantifiable value is needed to reflect the degree of contrast. This is the contrast to background noise ratio (CNR).

The intensity of the strand is set to be the targeted signal response. Similar to the first part of the experiment, a series of 10 regions of interest are taken consecutively along the length of the strand spacer material to sample this intensity. The sizes of these ROIs are much smaller than those used in the first part of the experiment. This serves to limit the ROIs to only encompassing the strand. These ROIs are 6 pixels wide and 4 pixels high which correspond to a sample dimension of 0.9 mm by 1.6 mm.

The background response is set to be the intensity response of the phantom material. A large rectangular region of interest is sampled as the background response by selected an area of the phantom that has a rough size of 20 pixels by 20 pixels, corresponding to a physical size of 3 mm by 8 mm.

A signal contrast-to-noise ratio (CNR) is then calculated using Equation 5.1. This equation calculates a separate CNR value for each ROI selected along the strand. The CNR value is a common quantification to use when determining the ability to discern different structures in the ultrasound [16].

$$CNR = \frac{m_s - m_b}{\sigma_b^2} \tag{5.1}$$

The factor m_s is the mean in intensity of the pixels within a ROI sampling the strand. The factors m_b and σ_b are the mean and standard deviation of the pixel intensities from the large ROI sampling the phantom. Each ROI along the sampled strand gives a separate CNR value. The mean and variance for the CNR values for the set of ROI for a single strand are calculated at the end. Note that the minor variation in strand intensity is not factored into this equation as average-reflected-power intensity responses vary in several orders of magnitude than respective responses in B-Mode images.

These CNR calculations are done for both B-Mode images and average-reflected-power images of regular strands and EchoStrands^{TM}.

5.3 Results

The B-Mode images of both regular and EchoStrands^{TM} in phantom at different strand orientations are shown in Figure 5.3. It is observed that the contrast between the strands and the

background noise of the phantom decreases as the strand is oriented at greater angles. The the regular strand's intensity decreases more rapidly as the strand orientation changes in comparison to the EchoStrand^{TM}. It is discernable over a much smaller range of strand orientations than the EchoStrand^{TM}. The change in strand intensity is minimal over the different orientations but the contiguity of the structure drastically decreases structure.

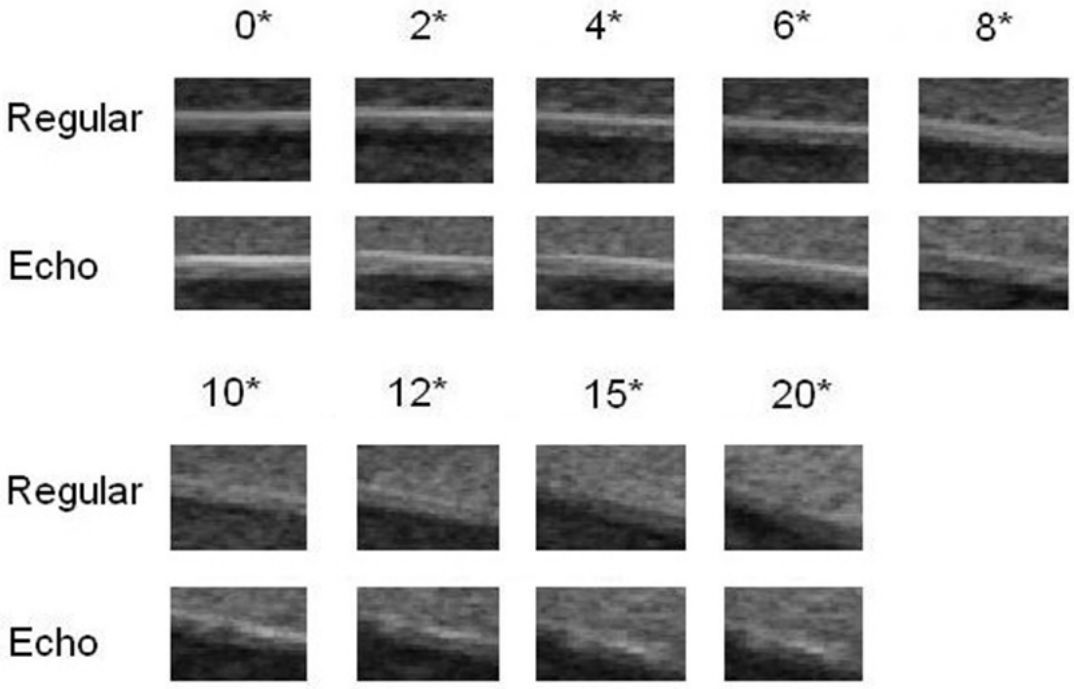

Figure 5.3: B-Mode images of short strand segments in phantom orientated at the indicated angles

Figure 5.4 shows the average-reflected-power images for both regular and EchoStrands^{TM} at different orientations. Similar to the results in the B-Mode, the EchoStrand^{TM} has better contrast and is more discernable over a greater range of strand orientations than regular strands. There is a drop in intensity as the strand is oriented at greater angles as well as a drop in contiguity but not to the degree found in B-Mode images.

The regular strand disappears for orientations greater than 15 degrees but the EchoStrands^{TM} are still visible up till 20 degree orientation in the average-reflected-power images.

The logs of the contrast-to-noise (CNR) ratios are plotted in Figure 5.5. The output agrees with our observations as there the CNR values for average-reflected-power images are much higher than traditional B-Mode imaging. In both imaging mediums, the CNR values decrease with increases angle.

The difference of CNR values between the strands in the B-Mode output is relatively similar

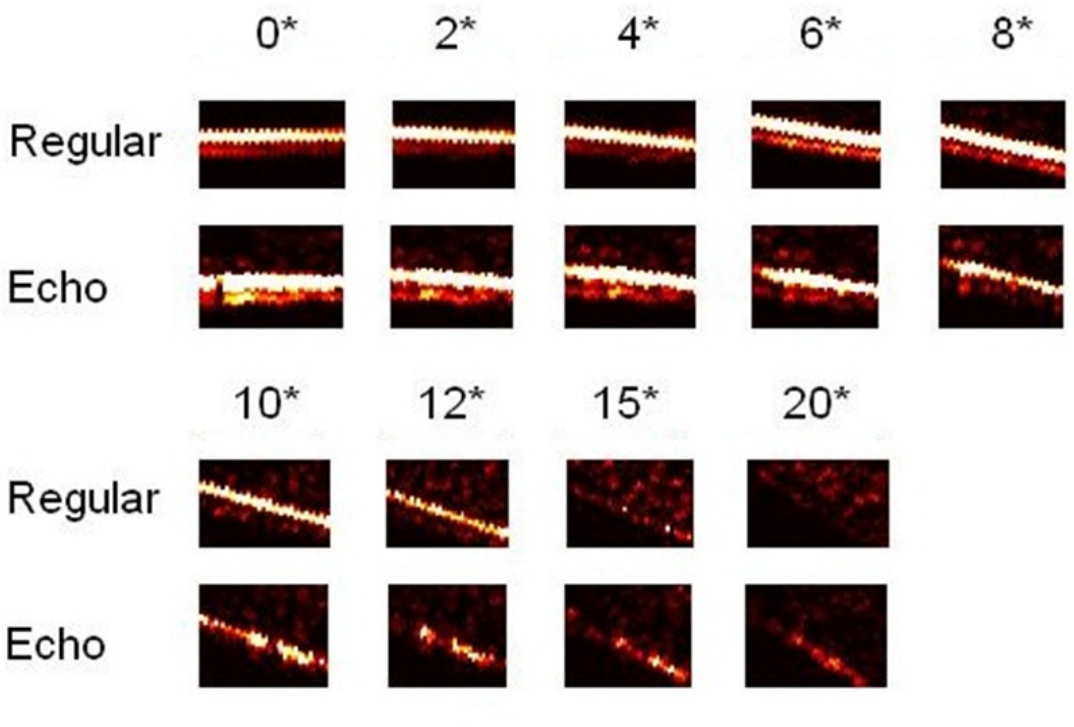

Figure 5.4: Average-reflected-power images of short strand segments orientated at the indicated angles

throughout though the EchoStrand^{TM} gives a slightly better response at non-parallel orientations than regular strands. The CNR for the average-reflected-power images shows more difference between the two strand types. At orientations lower than 10 degrees, the CNR values are relatively on par with each other. At greater than 10 degree orientations, however, the EchoStrand^{TM} is still able maintain a high CNR ratios while the regular strand's CNR is almost negligible.

The result of the CNR analysis agrees with the visual inspection of the images. Average-reflect-power imaging gives a much better contrast against background noise over B-Mode imaging. The EchoStrand^{TM} can be better contrasted against background noise than regular strands especially at non-parallel orientations.

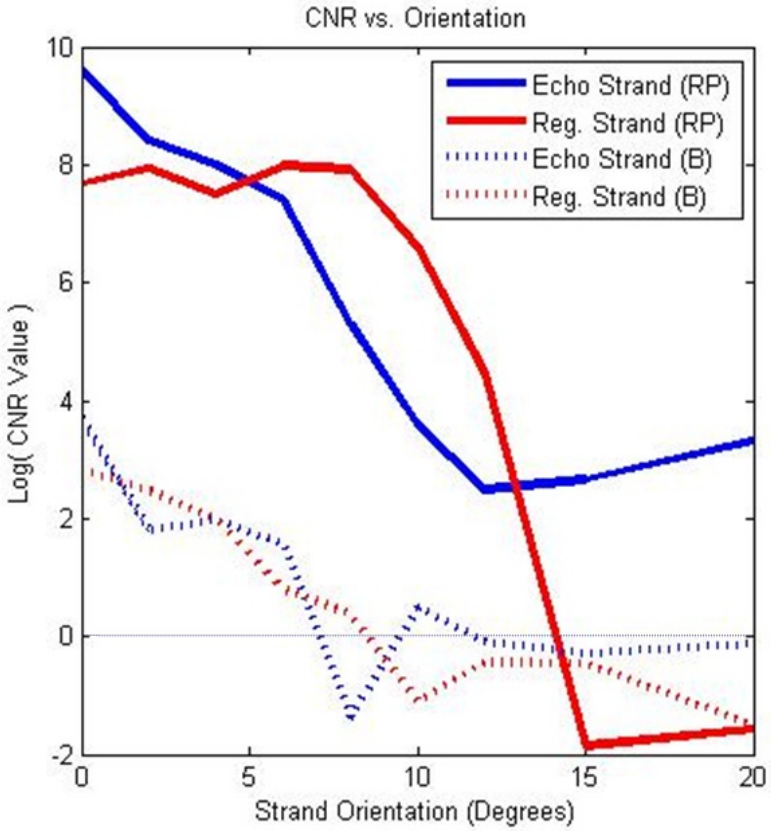

Figure 5.5: Log of contrast-to-noise (CNR) ratio plotted against the strand orientation for different imaging methods and EchoStrands^{TM} and regular strands.

Chapter 6

Discussions, Conclusions and Future Work

6.1 Discussions

Imaging Methods Based on the results from the contrast to noise analysis, average-reflected-power imaging allows for greater contrast between the image intensities of the strands versus the background noise, making it easier to localize the strands. This is also supported by visually comparing B-mode and average-reflected-power strand images from the experiment.

Strands are difficult to localize in a traditional B-Mode image due to applied thresholds and compressions that decrease the B-Mode image's dynamic range. The reason for these compressions is that B-Mode images are mainly used to delineate between tissues in the body which have very similar acoustic impedance factors. An example of this is the use of B-Mode imaging to delineate the boundary of the prostate. The compressed dynamic range of the B-Mode image enhances the contrast between the relatively similar tissues of the prostate and the surrounding area. In terms of strand localization, the acoustic impedance factor of the strand is very different from the surrounding tissue. The full extent of this difference can't be captured by traditional B-Mode imaging. The compressed contrast range of this imaging mode means that extremely strong ultrasound reflectors, like the strand, become saturated in B-Mode images, cutting short both their intensity and contrast.

Average-reflected-power is computed over the full range of the raw RF data. This allows it to capture the large contrast difference between strands and the surrounding tissue. Strands become more visible and easier to localize as a result. The drawback of this increased range is that the smaller contrast differences between the different tissue types become harder to discern. This limits the average-reflected-power method to localizing implanted seeds, strand and other objects that give extremely high intensity responses.

Strand Localization Looking at the sagittal image sweeps across the strand for different strand orientation, both strand types give similar responses at parallel orientations. At these orientations, both the EchoStrand^{TM} and regular strand gives a tight, tall intensity peak that falls off significantly after 2 to 3 degrees from the peak intensity. The peak corresponds to where the image plane is incident to the strand. The intensity response of the strand also varies along

its length and this uncertainty is represented by the error bars of the image sweep plot. At the parallel orientations, the error in intensity is relative small compared to the actual intensity value.

At strand orientations above six degrees, the EchoStrand^{TM} is still able to maintain a relatively high peak intensity response, though the peak is not as tight. The relative errors in peak intensity have also increased. The peak intensities of the regular strand at these orientations are now very low with extremely high error.

In terms of localizing strands across different image planes, it is much easier to localize those that have a high peak intensity with a small degree of error than those that have a low peak intensity with a large amount of uncertainty.

For example, based on the data in Figure 4.6, when attempting to determine if an EchoStrand^{TM} at zero degree orientation is on or close to the current image plane, we look for an intensity response corresponding to a IOD value of $8x10^6$ on a ROI along the strand. The image sweep plot tells us that the strand response is only this high when the strand is very close to the image plane. Contrast this to localization conducted on a regular strand with an orientation of 10 degrees. It is very hard to pick a intensity cut-off value in this case due to the short peak and the large error in the intensity values. Picking a value that account for the low end of the variation in peak intensity will cause the strand to be detected across a large number of image planes. It is therefore extremely hard to localize the regular strand at non-parallel orientations.

Intensity and CNR Both quantitative analysis and the phantom experiments show that both strand intensity and contrast to background decrease as the strands become less parallel. Intensity measurement on strand (Shown in Figure 4.6) in water shows a drop off of strand intensity between 0 to 8 degree orientations. At 8 degrees and above, the strand intensities remain relatively constant. For all orientations, the response of the EchoStrand^{TM} is higher than the regular strand.

Contrast to background noise (CNR) measurement (See Figure 5.5) indicates that the strand's contrast to noise ratio decreases with non-parallel orientations. The contrast to background noise between the two strand types are similar at low angled orientations but the EchoStrand^{TM} has a much higher CNR at high orientations than the regular strand.

Visual inspection of the B-Mode and RF images from both strands in water and strands in phantom supports the quantitative data. Both strands suffer a rapid decay in intensity with non-parallel orientations but the rate of decay is greater for the regular strand. The regular strand's contiguity also begins to break done at 8 degrees orientation and above resulting in large gaps appearing along the length of the strand.

In the phantom experiment, both the regular strand and the EchoStrand^{TM} are contrasted against the background at parallel strand orientations. However, due to the fact that the intensity of the regular strand is observed to decrease faster than the EchoStrand^{TM}, the regular strand is no longer discernable at orientations above 15 degrees. The EchoStrand^{TM} is still discernable

up till the 20 degree orientation.

The higher intensity response and contrast to background noise of the EchoStrands^{TM} indicate that it is a better candidate in strand localization. The most basic operation in segmenting the strands of interest from background noise is to apply a intensity threshold to the ultrasound image. With a higher strand intensity response, a high intensity threshold can be applied to the ultrasound image to segment out the strand allowing for more noise to be filtered. This results in a cleaner image for subsequent strand detection algorithms.

The better contiguity of the EchoStrand^{TM} over regular strands at non-parallel orientations also gives it another advantage. The contiguous strand outline allows for segmentation methods that take the strand's known shape into account. It is much easier to identify strands that appear as a solid line than ones that shows up in broken pieces. One of the major hurdles in localization implanted seeds is their small size [23]. Identifying a much larger, contiguous strand structure will overcome this problem.

Strand Materials The better intensity response and contiguity of the EchoStrand^{TM}, particularly at non-parallel orientations, may be attributed to the micro-bubbles embedded in the spacer material.

In regular strands, the core of the spacer material has a uniform composition. This means that the acoustic boundaries are only at the surface of the spacer material. However, the surface of the spacer material is smooth and flat meaning that mostly specular ultrasound reflections occur at this boundary. Based on the principles of specular reflection, it is expected that the intensity response of the regular strand becomes weaker when the strand has a non-parallel orientation as most of the echoes are directed away from the transducer.

With the EchoStrand^{TM}, the micro-bubbles within the spacer material create a set of internal reflective boundaries. These boundaries are formed by the change in acoustic impedance factor at the intersection between the spacer material and the gas inside the bubble. These sets of boundaries are irregular due to the tiny size of the micro-bubbles and allow non-specular reflection to occur. The echoes are scattered in all directions making the intensity response from these bubbles independent of orientation. This is one plausible reason why EchoStrand^{TM} gives a better response than regular strand at non-parallel strand orientations.

However, it is surprising that the presence of micro-bubbles does not significant improve the intensity of the EchoStrands^{TM}. These micro-bubbles have been observed in other experiments to result in much higher intensity responses[1, 17].

One explanation for low response is that the micro-bubbles are relatively few in number within the EchoStrand^{TM} material. Looking carefully at the strand, micro-bubbles are seen placed lengthwise along the strand in a single, roughly uniform column. If the number of these bubbles is to increase, a more intense response may result.

In addition, non-specular reflection scatters the incoming ultrasound beam. Scattered ultra-

sound beams travel in many different directs with only a few that are actually received by the transducer. This means that the non-specular responses generated by the micro-bubbles are much less intense than the specular reflections generated by the surface of the strand.

The reason why micro-bubbles are found to generate high intensity responses in other experiments is because those experiments use free-floating micro-bubbles. In those cases, the micro-bubbles have a very soft and flexible shell and is suspended in liquid. Incident ultrasound beams cause them to resonate in place. Their resonance then generates a series of intense ultrasound echoes that shows up intensely when imaged. However, this resonance is hampered if the shell of the micro-bubble is rigid[1, 5].

In the case of EchoStrands^{TM}, the strand material is extremely rigid and encases the entire micro-bubble. This prevents any resonance from taking place. If the micro-bubbles within the strand are allowed to float freely within the spacer material, then the intensity response is expected to be much higher. However, this environment is be extremely hard to create and maintain.

6.2 Conclusions

This experiment shows that average-reflected-power imaging is successful in enhancing the contrast of brachytherapy strands against a noisy background for both regular strands and EchoStrands^{TM} over a wide range of strand orientations.

The ultrasound intensity response and contrast to noise ratio of both strand types decrease at non-parallel strand orientations. However, the EchoStrand^{TM} gives a slightly higher intensity response across all orientations than the regular strand and maintains better contiguity in both B-Mode and average-reflected-power images. The EchoStrand^{TM} is also found to give better contrast against background noise than regular strands especially at non-parallel orientations.

The outcome of this experiment suggest that the used of both EchoStrands^{TM} and average-reflected-power imaging allows for better strand localization. Regular strands that aren't visible in traditional B-Mode due to noise or orientations can be successfully localized if replaced with EchoStrands^{TM} and imaged using average-reflected-power imaging.

6.3 Future Work

The promising results of this experiment indicate that detecting EchoStrands^{TM} with average-reflected-power imaging can be a valid technique in strand localization. Though the phantom used in this experiment roughly models the acoustic density of real tissue, it cannot simulate the wide range of calcification and structural patterns found in them.

A clinical experiment will have to be conducted to attempt to localize EchoStrands^{TM} using this technique on live patients. If the outcome of this clinical study proves fruitful, an intra-operative strand detection system can be designed to allow accurate strand localization and

real-time dosimetry to be incorporated into brachytherapy procedures.

Bibliography

[1] F. Calliada, R. Campani, O. Bottinelli, A. Bozzini, and M. G. Sommaruga. Ultrasound contrast agents basic principles. *Eur. J. of Radiology*, 27:S157–S160, 1998.

[2] B. J. Davis, J. F. Greenleaf, and et al. Measurement of the ultrasound backscatter signal from three seed types as a function of incidence angle: Application to permanent prostate brachytherapy. *Int. J. Radiation Oncology Biol. Phys.*, 57(4):1174–1182, 2003.

[3] D. French, J. Morris, M. Keyes, and S. Salcudean. Real-time dosimetry for prostate brachythearpy using trus and fluoroscopy. *MICCAI*, pages 983–991, 2004.

[4] P. Grimm and J. Sylvester. Advances in brachytherapy. *Rev. Urol.*, 6(suppl 4):S37–S48, 2004.

[5] L. Hoff, P. C. Sontum, and J. M. Hovem. Oscillations of polymeric microbubbles: Effect of the encapsulating shell. *J. Acoustic Society of America*, 107(4):2272–2280, 2000.

[6] L. Marrett, P. De, D. Dryer, and et al. *Canadian Cancer Society's Steering Committee: Canadian Cancer Statistics 2009*. Canadian Cancer Society, 2009.

[7] H. Matzkin, I. Kaver, and et al. Comparison between two iodine-125 brachytherapy implant techniques: pre-planning and intra-operative by various dosimetry quality indicators. *Radiotherapy and Oncology*, 68:289–294, 2003.

[8] S. A. McAleavey, D. J. Roubens, and K. J. Parker. Doppler ultrasound imaging of magnetically vibrated brachytherapy seeds. *IEEE Transactions on Biomedical Engineering*, 50:252–255, 2003.

[9] F. G. Mitri, P. Trompette, and J. Y. Chapelon. Improving the use of vibro-acoustography for brachytherapy metal seed imaging: A feasibility study. *IEEE Transactions in Biomedical Engineering*, 23:1–6, 2004.

[10] W. J. Morris, M. Keyes, D. Palma, and et al. Population-based study of biochemical and survival outcomes after permanent 125i brachytherapy for low- and intermediate-risk prostate cancer. *Oncology*, 10:860–865, 2009.

[11] S. Nag, D. Beyer, and et al. American brachytherapy society (abs) recommendations for transperineal permanent brachytherapy of prostate cancer. *Int. J. Radiation Oncology Biol. Phys.*, 44(4):789–799, 1999.

[12] S. Nag, W. Bice, and et al. American brachytherapy society recommendations for permanent prostate brachytherapy postimplant dosimetric analysis. *Int. J. Radiation Oncology Biol. Phys.*, 46(1):221–230, 2000.

[13] S. Nag, J. P. Ciezki, and et al. Intraoperative planning and evaluation of permanent prostate brachytherapy: Report of the american brachytherapy society. *Int. J. Radiation Oncology Biol. Phys.*, 51(5):1422–1430, 2001.

[14] A. V. Oppenheim. *Digital Signal Processing*. Prentice Hall, 1975.

[15] A. Patriciu, D. Petrisor, and et al. Brachytherapy seed placement under mri guidance. *IEEE Transactions on Biomedical Engineering*, 54:1499–1506, 2007.

[16] M. S. Patterson and F. S. Foster. The improvement and quantitative assessment of b-mode images produced by annular array/cone hybrid. *Ultrasonic Imaging*, 5:195–213, 1983.

[17] E. Quaia. Microbubble ultrasound contrast agents: an update. *Eur Radiol*, 17:1995–2008, 2007.

[18] R. G. Stock, J. Kao, and N. N. Stone. Penile erectile function after permanent radioactive seed implantation for treatment of prostate cancer. *The Journal of Urol.*, 165:436–439, 2001.

[19] R. G. Stock, N. N. Stone, M. Dahlal, and Y. C. Lo. What is the optimal dose for 125i prostate implants? a dose-response analysis of biochemical control ,posttreatment prostate biopsies, and long-term urinary symptoms. *Brachytherapy*, 1:83–89, 2002.

[20] R. G. Stock, N. N. Stone, A. Tabert, C. Iannuzzi, and J. K. DeWyngaert. A dose-response study for i-125 prostate implants. *Int. J. Radiation Oncology Biol. Phys.*, 41(1):101–108, 1998.

[21] N. M. Tole and H. Ostensen. *Basic Physics of Ultrasonographic Imaging*. World Health Organization, 2005.

[22] K. Wallner, J. Roy, and L. Harrison. Dosimetry guidelines to minimize urethral and rectal morbidity following transperineal i-125 prostate brachytherapy. *Int. J. Radiation Oncology Biol. Phys.*, 32(2):465–471, 1995.

[23] X.Wen, S. E. Salcudean, and P. D. Lawrence. Detection of brachytherapy seeds using ultrasound radio frequency signals. *Proc. of SPIE*, 6147:1605–7422, 2006.

[24] Y. Yu, Lowell L. Anderson, and et al. Permanent prostate seed implant brachytherapy: Report of the american association of physicists in medicine task group no. 64. *Med. Phys.*, 26(10):2054–2073, 1999.

[25] M. J. Zelefsky, Y. Yamada, and et al. Postimplantation dosimetric analysis of permanent transperineal prostate implantation: Improved dose distributions with an intraoperative computer-optimized conformal planning technique. *Int. J. Radiation Oncology Biol. Phys*, 48(2):601–608, 2000.